

Numerical analysis of size effect in RC beams scaled along height or length using elasto-plastic-damage model enhanced by non-local softening

I. Marzec¹, J. Tejchman¹ and Z. Mróz²

¹Gdansk University of Technology

Gdańsk-Wrzeszcz 80-233, Narutowicza 11/12, Poland

irek@pg.edu.pl, tejchmk@pg.edu.pl

²IPPT, Warsaw, Poland

zmroz@ippt.pan.pl

Abstract

Numerical simulation results of laboratory tests on reinforced concrete beams subjected to four-point bending for a separate variation of the height and length were presented. Due to the lack of a geometrical similarity, two major failure mechanisms were observed: flexural failure mechanism with plastic yielding of reinforcement and shear failure mechanism with two different modes: brittle diagonal tension and brittle diagonal shear-compression. The shear strength increased with increasing effective height and decreased with increasing shear span-effective height ratio. In simulations, the finite element method was used, based on a coupled elasto-plastic-damage constitutive model for concrete under plane stress conditions. The constitutive model was enhanced by integral-type non-locality in the softening regime to yield mesh-independent results. The bond-slip law was assumed between concrete and reinforcement. Two-dimensional numerical calculations under plane stress conditions satisfactorily reproduced both experimental shear strengths and failure mechanisms with one set of input parameters. In addition, the effect of different material constants on strength and fracture was comprehensively studied. Advantages and shortcomings of the numerical approach were discussed.

Keywords: size effect; finite element method; elasto-plasticity; damage mechanics; reinforced concrete; non-local theory

1. Introduction

The size effect is a fundamental phenomenon in concrete structures. It denotes that both the: 1) nominal structural strength (corresponding to the maximal load value reached in the loading process) and 2) material ductility (ratio between the energy consumed during the loading process after and before the stress-strain peak) always decrease with increasing member size under tension [1]. These two deformation process parameters are of major importance for the assessment of the member safety and its interaction with adjacent structural members. Concrete structures exhibit a strong transition from the snap-through response in the post-critical phase for small size members to the snap-back response (a catastrophic drop in strength related to a positive slope in a stress-strain softening branch) for large size members. There exist several size effect rules for concrete [1]-[3]. The most realistic is the combined energetic-statistical size effect rule proposed by Bazant [4] that is valid for geometrically similar structures. However, the formulation of rules of limit load sensitivity of concrete and reinforced concrete members relative to both size and arbitrary shape variations is required for engineering applications. This constitutes a more difficult class of problems requiring an analysis of different failure mechanisms.

The extensive experimental studies of a size effect were performed for RC beams that were geometrically similar. A strong size effect was experimentally observed in RC beams without shear reinforcement wherein diagonal shear-tensile fracture occurred in [5]-[14]. It was predominantly of the energetic type. The experimental diagonal failure cracks had in experimental tests similar paths and relative lengths at the maximum load independently of the beam size. The size effect was also observed in reinforced concrete beams with shear reinforcement [15]-[17]. In these experiments a diagonal shear-tensile fracture [15], [16] or crushing of a compressive zone [17] took place in concrete. Thus the use of stirrups did not suppress the size effect provided the longitudinal and vertical reinforcement yielding did not occur. The effect of the varying reinforcement ratio on the failure mode in RC beams was experimentally shown by Carpintieri et al. [18]. The observed failure mode changed from longitudinal reinforcement yielding, through diagonal tension to compressive zone crushing with increasing reinforcement ratio. However, only a few papers were devoted to a size effect in RC beams with independently varying heights and lengths (e.g. [19]).

In our earlier paper [20], the novel laboratory experiments were described that were carried out on longitudinally reinforced concrete beams without shear reinforcement subjected to four-point bending.

62 RC beams of separately varying height and length were experimentally analyzed to investigate the size
63 effect on a nominal strength and post-critical brittleness. Beams were scaled in the height direction in the
64 first test series and in the length direction in the second series. Due to lack of geometrical similarity, two
65 failure mechanisms were exhibited: flexural failure mechanism with plastic yielding of reinforcement
66 and brittle shear mechanism in concrete with dominant normal diagonal crack displacements (so-called
67 shear-tension failure mode) or with simultaneous significant normal and tangential diagonal crack
68 displacements (so-called shear-compression failure mode). Load-deflection diagrams and crack paths
69 were registered during experiments. The digital image correlation (DIC) technique was applied to
70 visualize strain localization on the concrete surface. In addition, the crack opening and crack slip
71 displacements on the beam surface were measured. The experimental results showed pronounced
72 differences as compared with strut-and-tie models following ACI [21] and Zhang and Tan [22]. The
73 alternative formulae based on the modification of these models slightly improved the agreement [20].
74

75 The goal of the present paper is to offer numerical simulations of the beam response by the finite element
76 (FE) model and to relate them to our laboratory tests on reinforced concrete beams subjected to four-
77 point bending (with respect to strength and fracture) by taking different failure mechanisms into account.
78 Usually, the size effect has been investigated in concrete and concrete structural elements that are
79 geometrically similar and exhibit the same failure mechanism. The attention was paid to the reproduction
80 of the: 1) size effect related to the beam strength, 2) fracture process and 3) failure modes of diagonal
81 tension and diagonal shear compression.

82
83 Two-dimensional (2D) finite element (FE) analyses under plane stress conditions were performed with
84 the coupled elasto-plastic-damage constitutive model for concrete. The damage (e.g. [23]-[25]) and
85 coupled elasto-plastic damage formulations (e.g. [26-33]) were widely used to describe the concrete
86 fracture behaviour under various loading conditions. The formulations presented a simplified isotropic
87 (e.g. [23]-[26]) or a more realistic anisotropic damage concept (e.g. [26], [27], [29], [30], [33]).
88

9 The formulation in the current paper was enhanced by a characteristic length of micro-structure with the
0 aid of integral-type non-locality in the softening regime. The non-local theory allows for reproducing
1 fracture patterns independently of the mesh for both localized and distributed cracking, and the numerical
2 results are insensitive to the finite element mesh size and alignment. The bond-slip rule between concrete
3 and reinforcement was assumed in FE analyses. The effect of different material constants on strength



94 and fracture was comprehensively studied. Our focus was on a relationship between tangential and
95 normal displacements along a critical diagonal crack in RC beams which failed in shear.

96
97 Recently, the analogous constitutive model has been successfully used in investigations of the size effect
98 and related fracture in geometrically similar concrete beams with basalt reinforcement [34]. This model
99 was also applied to RC concrete beams under mixed shear-tension failure [35] and composite RC-EPS
100 slabs under shear failure [36]. In the current paper, the constitutive model for concrete was slightly
101 improved.

103 2. Overview of experimental program

104 2.1 General information

105
106 The laboratory tests of four-point bending were conducted on rectangular concrete beams with
107 longitudinal steel ribbed bars without shear (vertical) reinforcement [20].

108
109 The beams were scaled along either the height D (series '1', Tab.1, Fig.1A,) or length l_{eff} (series '2',
110 Tab.1, Fig.1B). The thickness of all beams was $t=0.25$ m to avoid differences in the hydration heat effects
111 that are proportional to the member thickness. The beam deformation and failure were characterized by
112 two non-dimensional geometric parameters and one size parameter: $\eta_a=a/D$, $\eta_b=b/D$, $\eta_l=l_{eff}/D=2\eta_a+\eta_b$.

113 The reinforcement ratio $\eta_r=A_r/A_b$ was constant for the varying cross-sectional area A_b of the beam. The
114 concrete cover ($c=4$ mm) was large enough to prevent the bond failure of a splitting type. Thus, the
115 distance from the bar centre to beam bottom was always $c'=h-D=50$ mm. For two reinforcement layers,
116 this distance was $c'=75$ mm. The reinforcement location parameter $\eta_c=c'/D$ varied between 0.10-0.28
117 (series '1') or was fixed at 0.14 (series '2').

118
119 The beams of the series '1' were scaled along the effective height D in the proportion 1:2:4 with the
120 constant effective span length $l_{eff}=2700$ mm (Fig.1A, Tab.1). The beams were denoted as S1D18a108,
1 S1D36a108 and S1D72a108, where the symbol S1 denotes the series '1', D - the effective beam depth
2 in [cm] and a - the shear zone length in [cm]. The beam S1D36a108 ($D=360$ mm) was twice as high as
3 the beam S1D18a108 ($D=180$ mm) and twice as small as the beam S1D72a108 ($D=720$ mm). Thus, the
4 shear zone length a and bending zone length b (distance between two concentrated forces F) were
5 constant $a=1080$ mm and $b=540$ mm, respectively (Fig.1A). The shear span parameter $\eta_a=a/D$ was 1.5,

126 3 and 6, the length parameter $\eta_l=l_{eff}/D$ was 3.75, 7.5 and 15 and the bending span parameter $\eta_b=b/D$ was
127 0.75, 1.5 and 3. Each beam height h included 3 identical concrete specimens to verify the result
128 repeatability (indicated as: S1D18A108_1 - S1D18a108_3, S1D36a108_1 - S1D36a108_3 and
129 S1D72a108_1 - S1D72a108_3).

130

131 The beams of the series '2' had the same height ($D=360$ mm) but varying effective span length l_{eff} and
132 shear span a (the latter scaled in the proportion 1:2:3) (Fig.1B, Tab.1). The beams were denoted as
133 S2D36a36 ($a=360$ mm), S2D36a72 ($a=720$ mm) and S2D36A108 ($a=1080$ mm) with the length
134 parameter $\eta_l=l_{eff}/D=3.5, 5.5$ and 7.5 , the shear span parameter $\eta_a=a/D=1.0, 2.0$ and 3.0 and the bending
135 span parameter $\eta_b=b/D=1.5$. The longest beam from the series '2' (S2D36a108) had the same dimensions
136 as the beam from the series '1' denoted as S1D36a108. The beam S2D36a36 was as twice as short as the
137 beam S2D36a72 and the beam S2D36a108 was as twice as long as the beam S2D36a72. Each beam
138 included 2 identical members (denoted as: S2D36a36_1 - S2D36a36_2, S2D36a72_1 - S2D36A72_2,
139 S2D36a108_1 - S2D36a36_2).

140

141 In total 15 beams (series '1': 9 beams and series '2': 6 beams) were subjected to four-point bending. The
142 ratio of the shear span a to the effective height D varied from $\eta_a=a/D=1$ up to $\eta_a=6$, thus different failure
143 modes were expected to be developed. The ratio of the bending span b to the effective height D varied
144 from $\eta_b=b/D=0.75$ up to $\eta_b=3$ (series '1') and $\eta_b=1.5$ (series '2').

145

146 The reinforcement of all beams consisted of ribbed bars of the diameter $\phi=20$ mm with the mean yielding
147 stress of $\sigma_y=560$ MPa (class B500) and the modulus of elasticity of 205 GPa. The longitudinal
148 reinforcement ratio was designed as $\rho_L=1.4\%$ ($\rho_L=A_{SL}/(bD)$, A_{SL} – the cross-section area of longitudinal
149 reinforcement). Each beam size required a different number of bars depending on the effective depth D .
150 The beams of $D=18$ cm and $D=36$ cm had 2 and 4 bars in one layer, respectively. The beam of $D=72$ cm
151 had two layers with 4 bars i.e. 8 bars in total (Fig.1C). In order to avoid the anchorage zone failure,
152 hooked steel bars were used (Fig.1) with the anchorage length of 130 mm, 310 mm or 670 mm, depending
3 on the beam height.

4

5 Three accompanying tests were performed, including uniaxial compression of the concrete cubes
6 ($150\times150\times150$ mm³) and splitting tension and elastic compression of the concrete cylinders ($\phi=150$ mm
7 and $L=150$ mm). The measured average characteristic compressive strength on cubes was $f_c=61.5$ MPa.



158 Thus, the corresponding concrete class was C45/55. The average characteristic splitting tensile strength
159 was $f_t=3.21$ MPa. The measured average elastic modulus was $E=34.2$ GPa. The tests were performed
160 under displacement-controlled conditions. The steel loading plates were always used in order to avoid
161 local concrete crushing. Their area was always the same, i.e. 100×250 mm² ($l_a \times t$). The area of support
162 (bearing) plates ($l_b \times t$) had also the same size. During the test, the vertical force and displacements were
163 measured. The true deflection at the mid-span and support displacement were registered by means of
164 linear variable displacement transducers (LVDT's). The steel strains were traced with strain gauges
165 placed on reinforcement bars at the beam mid-span. The front side of the beam was prepared to track
166 cracks and to measure their width with a simple microscope. A detailed description including the crack
167 opening w and slip displacements δ were calculated based on measurements with a digital extensometer
168 of DEMEC type with the base of 100 mm. The measuring mesh consisting of equilateral triangles which
169 covered the area where a critical diagonal crack was expected to appear. The number of triangles varied
170 between particular series depending on the beam size. During tests, the elongation of triangle sides (AB,
171 AC and BC) was measured and the crack trajectory was registered.

172

173 2.2 Experimental results on strength and fracture

174

175 The shear strength of beams evidently decreased with increasing both parameters $\eta_a=a/D$ and $\eta_l=l_{eff}/D$.
176 It also decreased with increasing parameter η_b from 0.75 to 1.5 in beams with varying effective depth
177 and constant effective length. The shear strength's increase was extremely large (250%) in the range of
178 $\eta_a=1.0$ ($\eta_l=3.5$) and $\eta_a=1.5$ ($\eta_l=3.75$).

179

180 Two different failure mechanisms were observed in the RC beams (Fig.2): plastic flexural failure
181 mechanism characterized by reinforcement yielding for $\eta_a=6$ ($\eta_l=15$, $\eta_b=3$) (Fig.2a) and shear failure
182 mechanism in concrete for $\eta_a=1-3$ ($\eta_l=3.5-7.5$, $\eta_b=0.75-1.5$) (Figs.2b-f). For the lower value of $\eta_a=2-3$
183 ($\eta_l=5.5-7.5$, $\eta_b=1.5$), the so-called diagonal tension failure mode dominated (Figs.2b and 2d), i.e. the
184 normal displacements were always larger than the tangential displacements along the critical diagonal
5 crack. In the case of the lowest values of $\eta_a=1-2$ ($\eta_l=3.5-5.5$, $\eta_b=0.75-1.5$), so-called shear-compression
6 failure mode dominated (Figs.2c, 2e and 2f), i.e. the normal displacements were always smaller than the
7 tangential displacements in the top beam region of the critical diagonal crack. The distance between the
8 critical diagonal crack and beam support d_c related to the shear span a varied between $d_c/a=0.5$ for low
9 beams ($\eta_a=3$) up to as $d_c/a=0$ for high beams ($\eta_a=1$). For the RC beam S2D36a36, concrete spalling in



190 the compressive zone above the critical diagonal crack was also observed.

191

192 For high beams, the strut-and-tie models following ACI [20] and Zhang and Tan [21] overestimated the
193 shear strength for $\eta_a=1.5-2$ (by 20%-100%) and underestimated for $\eta_a=1$ (by 5%-25%). The difference
194 between the experimental and theoretical results by ACI and Zhang and Tan increased with decreasing
195 η_a . The alternative formulae [19] based on the modification of the strut-and-tie model significantly
196 improved the theoretical results in the range of $\eta_a=1.5-2$, but at the same time strongly worsened the
197 results for $\eta_a=1$.

198

199 The discrepancies between the experimental and theoretical results (based on the strut-and-tie models)
200 according to [19] were caused by: a) the varying strut widths and strut inclinations for all high beams
201 with $\eta_a=1-2$ and b) the different shapes of compressive struts for the beams with $\eta_a=2$. The clear
202 disadvantage of strut-tie models was that they were not able to distinguish between 2 different failure
203 modes in shear (diagonal tension and shear compression) which affected the beam strength to a different
204 grade.

205

206 **3. Numerical approach**

207 **3.1 Concrete description**

208

209 The coupled isotropic elasto-plastic-damage constitutive model was proposed for monotonic and cyclic
210 loading of concrete [35]-[39]. Plasticity and scalar damage were combined assuming the so-called strain
211 equivalence hypothesis [40]. The elasto-plasticity was defined in terms of the effective stress according
212 to

213

214

$$\sigma_{ij}^{eff} = C_{ijkl}^e \varepsilon_{kl} . \quad (1)$$

215

6 where σ_{ij}^{eff} is the effective stress tensor, C_{ijkl}^e denotes the elasticity tensor for the undamaged material
7 and ε_{kl} is the strain tensor. In an elasto-plastic regime, the failure surface was assumed as a combination
8 of two surfaces [41], [42]. In compression, the shear yield surface based on the linear Drucker-Prager
9 criterion with isotropic hardening and softening was used [43]

0

$$f_1 = q + p \tan \varphi - \left(1 - \frac{1}{3} \tan \varphi\right) \sigma_c(\kappa_1), \quad (2)$$

where q is the Mises equivalent deviatoric stress, p denotes the mean stress and φ is the internal friction angle. The evolution of material hardening/softening related to growing effective strain κ_1 was defined by the uniaxial compression yield stress $\sigma_c(\kappa_1)$. The internal friction angle φ was assumed as [43]

$$\tan \varphi = \frac{3(1 - r_{bc}^\sigma)}{1 - 2r_{bc}^\sigma}, \quad (3)$$

where r_{bc}^σ is the ratio between the biaxial compressive strength and uniaxial compressive strength ($r_{bc}^\sigma = 1.2$). The invariants q and p are

$$q = \sqrt{\frac{3}{2} s_{ij} s_{ij}} \quad \text{and} \quad p = \frac{1}{3} \sigma_{kk}, \quad (4)$$

where σ_{ij} is the stress tensor and s_{ij} denotes the deviatoric stress tensor. The flow potential was defined as

$$g_1 = q + p \tan \psi, \quad (5)$$

where ψ is the dilatancy angle ($\psi \neq \varphi$). For the sake of simplicity, the constant values of φ and ψ were assumed. In tension, the Rankine criterion was used with a yield function f_2 [41], [42] with isotropic softening defined as

$$f_2 = \max\{\sigma_1, \sigma_2, \sigma_3\} - \sigma_t(\kappa_2), \quad (6)$$

where σ_i – the principal stress, $\sigma_t(\kappa_2)$ – the tensile yield stress and κ_2 – the hardening/softening parameter equal to the maximum principal plastic strain ε_1^p . The associated flow rule was assumed. The edges and vertices in Rankine yield function were taken into account by the interpolation of 2-3 plastic multipliers according to the Koiter's rule. The same procedure was adopted in the case of combined tension (Rankine criterion) and compression (Drucker-Prager criterion). For both yield stress functions $\sigma_c(\kappa_1)$ and $\sigma_t(\kappa_2)$,

250 the linear hardening was assumed with the plastic hardening modulus $H_p = E/2$. The graphic
 251 interpretation of failure surface for the coupled Drucker-Prager-Rankine criterion is presented in Fig.3.

252

253 The material degradation was calculated within isotropic damage mechanics, independently in tension
 254 and compression using one equivalent strain measure $\tilde{\varepsilon}$ by Mazars [24] (ε_i - principal strains)

255

$$256 \quad \tilde{\varepsilon} = \sqrt{\sum_i \langle \varepsilon_i \rangle^2} . \quad (7)$$

257

258 The equivalent strain measure $\tilde{\varepsilon}$ may be defined in terms of elastic or total strains [41]. The stress-strain
 259 relationship was represented by the following formula

260

$$261 \quad \sigma_{ij} = (1 - D)\sigma_{ij}^{eff}, \quad (8)$$

262

263 with the term '1-D' defined as:

264

$$265 \quad (1 - D) = (1 - s_t D_t)(1 - s_c D_c), \quad (9)$$

266 where

$$267 \quad D_t = 1 - \frac{\kappa_0}{\kappa_t} \left(1 - \alpha + \alpha e^{-\beta(\kappa_t - \kappa_0)} \right), \quad (10)$$

$$268 \quad D_c = 1 - \left(1 - \frac{\kappa_0}{\kappa_c} \right) \left(0.01 \frac{\kappa_0}{\kappa_c} \right)^{\eta_1} - \left(\frac{\kappa_0}{\kappa_c} \right)^{\eta_2} e^{-\delta_c(\kappa_c - \kappa_0)}, \quad (11)$$

$$269 \quad s_t = 1 - a_t \omega(\sigma_{ij}^{eff}) \quad \text{and} \quad s_c = 1 - a_c \left(1 - \omega(\sigma_{ij}^{eff}) \right), \quad (12)$$

$$270 \quad \kappa_t = \kappa \omega(\sigma_{ij}^{eff}) \quad \text{and} \quad \kappa_c = \kappa \left(1 - \omega(\sigma_{ij}^{eff}) \right), \quad (13)$$

$$271 \quad \omega(\sigma_{ij}^{eff}) = \begin{cases} 0 & \text{if } \sigma_i^{eff} = 0 \\ \frac{\sum \langle \sigma_i^{eff} \rangle}{\sum |\sigma_i^{eff}|} & \text{otherwise} \end{cases} . \quad (14)$$

2

3 The damage functions D_t and D_c describe the damage evolution under tension [44] and compression [45]
 4 by means of the following material constants: α , β , η_1 , η_2 and δ_c . The threshold parameter κ was defined
 5 as the maximum of the equivalent strain measure $\tilde{\varepsilon}$ reached during the load history up to time t : $\kappa(t) =$
 6 $\max_{\tau < t} \tilde{\varepsilon}(\tau)$. In contrast to our previous constitutive concrete model [35]-[39], the damage under tension

277 was here separately controlled in FE simulations by the threshold parameter κ_t and the damage under
 278 compression separately by the threshold parameter κ_c . The damage function under tension D_t solely
 279 evolved for the threshold parameter $\kappa_t \geq \kappa_0$ and the damage function under compression D_c evolved
 280 only for the threshold parameter $\kappa_c \geq \kappa_0$. For the threshold parameters $\kappa_t \leq \kappa_0$, $\kappa_c \leq \kappa_0$, there was no
 281 damage growth under tension and compression ($D_t = D_c = 0$). The splitting factors are a_t and a_c , and
 282 $\omega(\sigma_{ij}^{eff})$ denotes the stress weight function [46]. Thus, under pure tension the stress weight function was
 283 $\omega(\sigma_{ij}^{eff}) = 1$ and the growth of damage under pure tension was solely influenced by the evolution of D_t .
 284 The Mac Cauley bracket in Eq.14 is defined as $\langle x \rangle = (x + |x|)/2$. The constitutive model with a
 285 different stiffness in tension and compression and a positive-negative stress projection operator to
 286 simulate crack closing and crack re-opening is thermodynamically consistent. It shares main properties
 287 of the model by Lee and Fenves [46], which was proved to be consistent with thermodynamic principles
 288 (plasticity is defined in the effective stress space, isotropic damage is used and the stress weight function
 289 is continuous). Carol and Willam [47] showed that for damage models with crack-closing-re-opening
 290 effects, only isotropic formulations did not suffer from spurious energy dissipation under non-
 291 proportional loading in contrast to anisotropic ones.

292

293 Due to the small thickness of beam, the plane stress condition (out of plane stress components equal to
 294 zero) was a natural choice for numerical modelling. In plasticity the plane stress-projected method was
 295 used and the plane stress elasticity matrix was applied in the analysis. For calculations of the equivalent
 296 strain measure, the out-of-plane normal strain was determined. In tension, the result differences between
 297 plane strain and plane stress were negligible. In compression, the strength for plane strain state was higher
 298 by about 20% than for plane stress state due to the presence of the out of plane stress.

299

300 In the case of linear hardening model, the following 16 material constants are required: E , ν , κ_0 , α , β , η_1 ,
 301 η_2 , δ_c , a_t , a_c , ψ , φ , initial yield stresses σ_{yt}^0 (tension) and σ_{yc}^0 (compression) and plastic hardening moduli
 302 H_p (in compression and tension). The quantities σ_{yt}^0 (initial yield stress during hardening) and κ_0 are
 3 responsible for the peak location on the stress-strain curve and a simultaneous activation of the plasticity
 4 and damage criteria. The shape of the stress-strain curve in softening is influenced by the constant β in
 5 tension, and by the constants δ_c and η_2 in compression. The stress-strain curve at the residual state is
 6 affected by the constant α in tension and by the constant η_1 in compression. Since the compressive
 7 stiffness is recovered upon the crack closure as the load changes from tension to compression, and the



308 tensile stiffness is not recovered due to compressive micro-cracks, the damage splitting factors a_c and a_t
309 may be taken for the sake of simplicity as $a_t=0$ and $a_c=1.0$. The equivalent strain measure $\tilde{\epsilon}$ (Eq.7) was
310 defined in terms of total strain following [40]. A simple cyclic tension-compression-tension element test
311 was performed to show the model response under the load reversal (Fig.4). The 1D concept of the
312 stiffness recovery with the limit damage splitting factors a_t and a_c (value 0 or 1) was shown in Fig.4a.
313 Figure 4b presents the stress-strain curves for two full load cycles with three different sets of the damage
314 splitting factors ($a_t=0$ and $a_c=1.0$, $a_t=0$ and $a_c=0.8$ and $a_t=0.2$ and $a_c=1.0$). The load began in tension,
315 next it changed to compression (below the compressive strength), then back to tension and finally to
316 compression (above the compressive strength) and tension. The stress-strain diagrams for two different
317 loading scenarios are shown in Fig.4c with the damage splitting factors $a_t=0.2$ and $a_c=0.8$. For the first
318 loading scenario (blue curves), the load started in tension (curve '1'), then it moved to compression above
319 the strength limit (curve '2') and next back to tension (curve '3'). For the second loading scenario (red
320 curves), the load started in compression below the compressive strength (curve '1'), next moved to tension
321 above the tensile strength (curve '2'), and then back to compression above the compressive strength (curve
322 '3') and to tension (curve '4').

323

324 The results of Fig.4 show the different stiffness degradation in compression and tension (the degradation
325 was stronger in tension). The effect of the damage splitting factors a_t and a_c on the stress-strain diagram
326 under tension-compression-tension-compression was more noticeable in compression (Fig.4b). The
327 compressive stiffness was recovered upon the crack closure as the load moved from tension to
328 compression, and the tensile stiffness was not recovered as the load moved from compression to tension
329 due to crushing micro-cracks with $a_c=1$ and $a_t=0$ (Fig.4b). For $a_c=0.8$ and $a_t=0$ (Fig.4b), a decrease of
330 the factor a_c from 1.0 to 0.8 lead to a not-full recovery of the compressive stiffness in a transition from
331 tension to compression. An increase of the factor a_t from 0.0 to 0.2 ($a_t=0.2$ and $a_c=1.0$, Fig.4b) contributed
332 to the slightly larger tensile stiffness during a transition from compression to tension. The influence of
333 stiffness degradation due to compressive cracks is seen in Fig.4c ($a_t=0.2$ and $a_c=0.8$). When the load
334 moved from compression to tension (red curve '2'), the tensile stiffness was not fully recovered due to
5 damage in compression. The compressive stiffness was not also fully recovered during a transition from
6 tension to compression (blue curve '2'). The constitutive model was carefully validated in element tests
7 [37], e.g. for uniaxial cyclic compression and four-point cyclic bending under tensile failure (Fig.5). The
8 results of numerical calculations during cyclic element tests were in satisfactory agreement with the
9 experimental outcomes [48], [49] (Fig.5).

0



341 Figure 6 shows the stress-strain diagrams under cyclic uniaxial tension and cyclic uniaxial compression
342 for the different important material constants η_2 , δ_c , β , and κ_0 (which were independently changed). The
343 stress-strain results indicate that the parameter κ_0 is responsible for a peak location and a simultaneous
344 activation of plastic and damage criteria. The parameter β affects model response in softening during
345 tension and parameters δ_c and η_2 affect model response in softening during compression. In addition the
346 parameter η_2 affects the hardening curve in compression. The effect of two other parameters (α and η_1)
347 describing the stress-strain curve at the residual state is negligible.

348

349 The material constants E , ν , κ_0 , β , α , η_1 , η_2 , δ_c and two hardening yield stress functions should be
350 determined for concrete by means of two independent simple monotonic tests: uniaxial compression test
351 and uniaxial tension (or three-point bending) test for the already fixed damage splitting factors a_t and a_c .
352 The precise determination of the damage scale factors a_t and a_c requires one full cyclic compressive test
353 and one full cyclic tensile (or three-point bending) test. In addition, the values of φ and ψ can be
354 determined from triaxial compression tests [40]. The material constants were fitted to the experimental
355 uniaxial compressive strength of concrete $f_c=61.5$ MPa, experimental tensile strength of concrete
356 cylinders during splitting tension $f_t=3.2$ MPa and experimental modulus of elasticity of $E=34$ GPa. Due
357 to the lack of laboratory full stress-strain curves during uniaxial compression and uniaxial tension, the
358 tensile G_f and the compressive fracture energy G_c were assumed based on the literature data. The
359 following set of the material parameters was thus assumed for monotonic FE calculations: $E=34$ GPa and
360 $\nu=0.2$, $\sigma_{yt}^0 = 3.3$ MPa, $\sigma_{yc}^0 = 60$ MPa, $H_p=17$ GPa, $\kappa_0=9\times 10^{-5}$, $\phi=14^\circ$ [40], $\psi=8^\circ$, $\beta=85$, $\alpha=0.95$,
361 $\eta_1=1.15$, $\eta_2=0.15$ and $\delta_c=150$ with $a_t=0$ and $a_c=1$. Using the assumed material constants, the tensile
362 fracture energy was $G_f=100$ N/m (typical value for concrete) and compressive fracture energy
363 $G_c=4000$ N/m ($G_c/G_f=40$). The concrete behaviour during simple cyclic element tests in uniaxial
364 compression, tension and simple shear with the assumed material parameters is shown in Fig.7. The
365 calculated maximal uniaxial compressive strength was $f_c=60$ MPa (Fig.7a), maximal uniaxial tensile
366 strength was $f_t=3.2$ MPa (Fig.7b) and maximal shear strength was $\tau_{max}=11$ MPa ($\tau_{max}\approx\sqrt{f_c f_t}$) (Fig.7c).

367

8 3.1 Non-local approach

9

0 Standard constitutive laws are not able to describe properly strain softening of the material when using
1 FEM that results in pathological sensitivity of the numerical solution to the size and alignment of finite
2 elements. Since these laws contain no information about the size and spacing of localization zones, their

373 enrichment by a characteristic length of micro-structure (related to the size and spacing of material
 374 heterogeneities) is necessary. The characteristic length restores also the well-posedness of boundary
 375 value problems and makes the FE results mesh-independent. An integral-type non-local theory in the
 376 integral format was used as a regularization technique in order to describe properly strain localization
 377 and to capture a deterministic size effect (dependence of the nominal strength on the structure size) [50]-
 378 [53]. In this approach, the principle of local action does not hold. The introduction of non-locality does
 379 not violate thermodynamic principles [54]. In the calculations the equivalent strain measure the $\tilde{\epsilon}$ in
 380 damage region was replaced by its non-local definition $\bar{\epsilon}$ [55]

381

$$382 \quad \bar{\epsilon} = \frac{\int_V w(\|\mathbf{x} - \boldsymbol{\xi}\|) \tilde{\epsilon}(\boldsymbol{\xi}) d\boldsymbol{\xi}}{\int_V w(\|\mathbf{x} - \boldsymbol{\xi}\|) d\boldsymbol{\xi}} . \quad (15)$$

383

384 The Gauss distribution function was used as a weighting function w [50]

385

$$386 \quad w(r) = \frac{1}{l_c \sqrt{\pi}} e^{-\left(\frac{r}{l_c}\right)^2} , \quad (16)$$

387

388 where l_c is a characteristic length of micro-structure and the parameter r denotes the distance between
 389 material points. The averaging in Eq.16 was restricted to a small representative area around each material
 390 point (the influence of points at the distance of $r=3 \times l_c$ was only of 0.01%). The function in Eq.15 satisfies
 391 the normalizing condition [50]. In order to accelerate the calculations, the non-local averaging was
 392 performed solely in the neighbourhood of integration points (limited to the distance of $3l_c$). Different
 393 techniques (e.g. symmetric local correction approach, distance-based and stress-based model) may be
 394 used to calculate softening non-local parameters near boundaries in order to remove an excessive energy
 395 dissipation (particularly pronounced for notched specimens) [55], [56]. The distance-based model seems
 396 to be the most realistic since it provides a good agreement for both unnotched and notched beams with
 397 the same set of parameters [56]. When calculating non-local quantities close to notches the so-called
 8 “shading effect” is considered [51], i.e. the averaging procedure considers the notches as an internal
 9 barrier that is shading a non-local interaction. In the case of a symmetry-axis, the material points on the
 0 other side of the symmetry axis are also considered (a mirror reflection is taken into account at the
 1 distance of $3 \times l_c$). The objectivity of numerical results for RC structural elements within the non-local

402 approach was shown in [57] and [58]. The 3D calculation results within the non-local approach were
403 demonstrated e.g. in [35], [41], [42], [67].

404

405 The characteristic length l_c is mainly determined with an inverse identification process of experimental
406 data [59], [60]. The measured width of the localization zone in plane and reinforced concrete beams
407 under bending was about $w_{lz} \approx 3.5$ mm (0.25 times the maximum aggregate size and 1.5 times the mean
408 aggregate size) on the beams' surface based on the digital image correlation (DIC) results [61]. The
409 characteristic length l_c of micro-structure should be thus assumed for concrete within isotropic elasto-
410 plasticity and isotropic damage mechanics as about $l_c = 1.2-1.5$ mm. i.e. $l_c \approx 3w_{lz}$ [57], [60]. In order to
411 obtain totally mesh-independent results, the element mesh size s_e should be smaller or equal to $s_e = \leq 2 \times l_c$
412 [57], [60]. The numerical results of strain localization in different RC structural elements (beams,
413 columns, walls, corbels) by using a non-local approach in softening were discussed among others in [34]-
414 [36], [41], [42], [57], [58], [62]. The numerical results indicated that for greater l_c , the higher were both
415 strength and ductility of concrete members. The calculations with $l_c = 1.2-1.5$ mm would essentially
416 lengthen the computation time. Therefore we have assumed $l_c = 5$ mm in our FE analyses that is a limit
417 value in order to obtain realistic results of the location and inclination of localized zones in concrete
418 members [57].

419

420 3.2 Description of reinforcement and bond-slip law

421

422 In order to simulate the behaviour of steel bars, an elastic-perfectly plastic constitutive model was
423 assumed with the modulus of elasticity of $E_s = 205$ GPa and yield stress of $\sigma_y = 560$ MPa. All
424 longitudinal bars were modelled as one-dimensional truss elements. For describing the interaction
425 between concrete and reinforcement, a bond-slip law was defined. The interface with a zero thickness
426 was assumed along a contact line where a relationship between the shear traction and slip was introduced.
427 In general, this relationship is complex and depends on several factors (e.g. concrete class, concrete
428 cover, bar diameter, bar rib height and bar rib spacing). Two different bond-failure mechanisms may
9 appear connected to a pull-out or splitting mode. The relationship between the bond shear stress τ and
0 slip δ followed CEB-FIP Code [63] (Fig.8). This bond-slip law describes 4 different phases by taking
1 hardening/softening into account in the relationship. A similar bond-slip relationship was presented in
2 [64], based on a local fracture energy approach following earlier extensive research works on the bond-
3 slip behaviour. We assumed the following basic bond values in FE simulations: $\tau_{max} = 10$ MPa, $\tau_f = 3$ MPa,



434 $\delta_1=1$ mm, $\delta_2=2$ mm, $\delta_3=5$ mm and $\alpha=0.2$ (Fig.8), based on our pull-out tests in the concrete block with
 435 steel bars of the diameter $\phi=12$ mm [34], [65] (the pull-out tests with steel bars of $\phi=20$ mm were not
 436 carried out). Since the calculated bond stresses τ_b were clearly below τ_{max} (based on preliminary
 437 simulations), the effect of the bar diameter ϕ on τ_{max} was neglected, thus

438

$$439 \quad \tau_b = \begin{cases} \tau_{max} \left(\frac{\delta}{\delta_1} \right)^\alpha & 0 < \delta \leq \delta_1 \\ \tau_{max} & \delta_1 < \delta \leq \delta_2 \\ \tau_{max} - (\tau_{max} - \tau_f) \frac{\delta - \delta_1}{\delta_3 - \delta_2} & \delta_2 < \delta \leq \delta_3 \\ \tau_f & \delta_3 < \delta \end{cases} . \quad (17)$$

440

441 In addition, the calculations were carried out with the different parameters δ_1 (Fig.8) and perfect bond.
 442 The constitutive model for concrete was implemented into the commercial finite element code Abaqus
 443 [43]. The non-local averaging was performed in the current configuration. This choice was governed by
 444 the fact that element areas in this configuration were automatically calculated by Abaqus [43]. Due to
 445 the access lack to information on integration points stored internally by Abaqus, a special technique was
 446 applied to perform non-local averaging by means of the UMAT (user constitutive law definition)
 447 subroutine. Two FE-meshes with the identical topology (on the same set of nodes) were defined. The
 448 finite elements from the first mesh were first called in an iteration (they had lower labels). They gathered
 449 information about coordinates of integration points, current total strains (to calculate equivalent strains)
 450 and a volume associated with integration points. They had no stiffness and always returned a zero force
 451 vector, so they did not affect the FE results. Next the finite elements from the second mesh (with higher
 452 labels) were called. They used the information gathered by elements from the first mesh (and stored in a
 453 globally accessed Fortran variable) to calculate non-local quantities and return a stress vector.

454

455 **4. Comparison between FE model responses and test results**

456

7 The FE analyses were performed for experimental reinforced concrete beams under plane stress
 8 conditions. In the FE calculations, some simplifications were assumed. First, 2D calculations were
 9 carried out and the half part of beams was analyzed only (Fig.9) in order to strongly reduce the
 0 computation time. Thus, a symmetric failure mode was taken into account in contrast to the experimental
 1 results. In order to capture a statistical size effect, the full beam should be taken into account with a

462 statistical distribution of the concrete tensile strength using a correlated random field [65]. However, the
463 effect of a statistical distribution of the concrete tensile strength on the location of the critical diagonal
464 crack was insignificant [65].

465

466 In the present simulations, the 2D meshes consisting of 57,700-203,500 plane stress triangular elements
467 with linear shape functions in the so-called 'union jack pattern' were used to avoid locking (Fig.9). The
468 size of quadrilateral elements was very small ($s_e=5$ mm) and was equal to $l_c=5$ mm (Fig.9).

469

470 **4.1 Force-displacement curves**

471

472 The FE results of force-displacement curves were compared to the experiments in the plots of Fig.10 (for
473 $\eta_a=1-6$). The experimental ultimate vertical forces were well reproduced in the FE analyses for the same
474 failure mode (Tab.2). The maximum difference was 0.5-7.5% (Tab.2). The largest difference was for the
475 highest beam S2D36a72_2 ($\eta_a=2$) - 7.5% (Fig.10e). Note that both the shear-tension failure and shear-
476 compression failure might occur in the experiment for $\eta_a=2$. However, in the FE calculations, the shear-
477 compression failure was solely reproduced for this beam. Therefore the calculated shear strength for
478 S2D36a72_1 ($\eta_a=2$) was significantly too high (47.4%) due to the different failure mode (Fig.10e). The
479 softening (post-peak) modulus, calculated as the inclination tangent of the force-deflection curve to the
480 horizontal after the peak force, defined as $E_s = |\Delta F / \Delta u|$, (Fig.10) increased with decreasing parameter
481 η_a for $\eta_a \leq 3$, from $E_s=40-230$ kN/mm for $\eta_a=3$ up to $E_s=1400-1600$ kN/mm for $\eta_a=1-1.5$.

482

483 In the numerical analyses, the mobilized bond stress τ_b between concrete and reinforcement (Eq.17,
484 Fig.8) was located always on the hardening curve of Fig.8 below the plateau ($\tau_b < \tau_{max}$). The maximum
485 bond stress was between 7-8 MPa (large beams) and 4-6 MPa (small beams), i.e. $< \tau_{max}=10$ MPa.

486

487 Figure 11 presents the calculated shear strength $\tau_c = V_{max} / (tD)$ ($V_{max} = 0.5F_{max}$) with increasing parameters
488 η_a and η_l as compared to the experimental values. The calculated results were also compared with the
9 shear strength according to our strut-and-tie model, being an improved alternative to the ACI approach
0 [21] (the model was described in [20])

1

492

$$\tau_c = \frac{1 - \eta_c}{\eta_a} \frac{\rho_l f_y [\eta_a^2 + (1 - \eta_c)^2]}{\eta_a^2 + (1 - \eta_c)^2 + \frac{1}{2\eta_c} \frac{\rho_l f_y}{f_c} (1 - \eta_c)^2}, \quad (18)$$

493

494 where f_y - the yield stress in reinforcement.

495

496 The agreement between the numerical and experimental results is satisfactory. The effective failure stress
 497 τ_c increased with increasing depth D due to a different failure mode but decreased with increasing span
 498 ratio η_a . In the series '1', the mean experimental value was $\tau_c=1.34$ MPa ($\eta_a=6$), $\tau_c=1.35$ MPa ($\eta_a=3$) and
 499 $\tau_c=2.86$ MPa ($\eta_a=1.5$) for the beams S1D18a108, S1D36a108 and S1D72a108 (the numerical values
 500 were: 1.36 MPa, 1.39 MPa and 3.15 MPa, respectively) (Fig.11). In the series '2', the measured shear
 501 strength decreased with increasing shear span a and effective length l_{eff} from $\tau_c=7.39$ MPa ($\eta_a=1$) to
 502 $\tau_c=2.11$ MPa ($\eta_a=2$) and next to $\tau_c=1.31$ MPa ($\eta_a=3$) for the beams S2D36a36, S2D36a72 and S2D36a108
 503 (the numerical values were: 7.26 MPa, 2.62 MPa and 1.39 MPa, respectively) (Fig.11). Equation 18
 504 yielded the realistic shear strength results in the range of $\eta_a \geq 1.5$ as compared to the experimental and
 505 numerical outcomes. However, for $\eta_a=1$ it provided a too small assessment of the shear strength.

506

507 **4.2 Strain localization zones**

508

509 Figures 12 and 13 show the contours of the non-local equivalent strain measure $\bar{\epsilon}$ (Eq.15) with the
 510 attached scale as compared with the experimental cracks pattern (marked as lines). The experimental
 511 critical diagonal crack was marked by the red arrow and the numerical critical diagonal localization zone
 512 was marked by the yellow arrow. For the sake of clarity, the longitudinal steel bars were removed. The
 513 calculated strain localization zones were obviously symmetric in contrast to the experimental cracks
 514 (Figs.12 and 13). However the overall characteristic of failure modes (reinforcement yielding or concrete
 515 shear mechanism) was satisfactorily reflected in calculations. The geometry of localized zones from FEM
 516 satisfactorily matched the experimental crack pattern (Figs.12 and 13), although some differences
 7 existed. In general, the differences became greater with decreasing η_a . The critical localized zone was
 8 too curved for the beam S1D36a108 ($D=360$ mm, $\eta_a=3$). The critical localized zone was located too close
 9 to the support for S1D36a108 ($D=360$ mm, $\eta_a=3$) and too far from the support for S1D72a108 ($D=720$
 0 mm, $\eta_a=1.5$), S2D36a72_1 ($L_{eff}=1980$ mm, $\eta_a=2$) and S2D36a36 ($L_{eff}=1260$ mm, $\eta_a=1$).

1

522 The calculated inclination of the critical diagonal localized zone ($\eta_a \geq 2$) matched well the mean
523 experimental crack values (Fig.14). However for $\eta_a \leq 1.5$ it was slightly too steep (47-49° against 42-43°).
524 Note that due to 2D simulations, 3D effects (expressed by concrete spalling due to the high horizontal
525 compressive force ($\eta_a = 1$), Fig.13c) could not be modelled.

526

527 The number of localized zones in FE simulations was slightly higher than in experiments. The average
528 spacing of calculated localized zones (main and secondary) along the beam bottom was smaller by about
529 9-27% as compared with the experimental average crack spacing (main and secondary) (Tab.3). The
530 highest differences were about 27% for beam S2D36a36 (Fig.13c) and 20% for beam S1D72a108
531 (Fig.12c). They were caused by the fact that the assumed tensile fracture energy was too high; the smaller
532 tensile fracture energy increased the crack spacing (see Section 5.1, Figs.18 and 19).

533

534 The experimental mean normalized height of the compressive zone at the beam top h_c/D in the shear and
535 bending domain against η_a prior to the failure as compared to the numerical results is described in Fig.15.
536 The agreement between experimental and numerical results is satisfactory. In the shear domain, the
537 experimental height h_c varied from 5 cm up to 7 cm and in numerical calculations from 4.8 up to 9.2 cm.
538 The highest difference was for $\eta_a = 1$. In the bending domain, the experimental height h_c varied from
539 8.5 cm up to 30 cm in comparison in view of 9 cm up to 25 cm in calculations. The highest difference
540 was for $\eta_a = 1.5$.

541

542 **4.3 Displacements along critical diagonal crack**

543

544 The calculated surface displacements along the mid-line in the critical diagonal localization zone (Figs.16
545 and 17) were only qualitatively compared with the experimental crack displacements due to two facts: a)
546 the displacements were calculated at slightly different points than the measured ones due to differences
547 between FE analyses and experiments and b) the displacement calculations were carried out within
548 continuum mechanics while the discrete cracks occurred in experiments (thus a direct comparison was
9 not possible). The comparison was performed for the beam S1D36a108 (with the diagonal shear-tension
0 failure mode) (Fig.16) and S1D72a108 (with the diagonal shear-compression failure mode) (Fig.17) for
1 two points along the critical shear zone. In addition, the evolution of the critical crack/localization zone
2 width along its length was presented in Fig.18 for the beams S1D36a108 and S1D72a108, based on the

553 results at three points along the crack length (at reinforcement, at the beam mid-height and at the upper
554 beam part).

555

556 In the case of the beam S1D36a108 ($\eta_a=3$), the normal displacement ω along the entire critical diagonal
557 localized zone was larger than the tangential displacement δ (Fig.16) that was consistent with our
558 experimental outcomes [19]. For the beam S1D72A108 ($\eta_a=1.5$), the tangential crack displacement δ
559 was higher than the normal one ω along the critical diagonal localized zone in the upper beam region
560 (Fig.17) as in the experiments [19]. The calculated widths of the critical localization zone were smaller
561 than the experimental widths of the critical crack for both the beams (Fig.18).

562

563 **5. Parametric numerical study**

564 **5.1 Effect of different material constants of concrete**

565

566 The impact of the different material constants on the behaviour of reinforced concrete beams is shown
567 for the beam S1D36a108 ($\eta_a=3$) (Fig.19) and beam S1SD72a108 ($\eta_a=1.5$) (Fig.20). The different
568 material constants were assumed, which controlled the damage under tension ($\beta=60$ instead of $\beta=85$),
569 damage under compression ($\eta_2=0.20$ and $\delta_c=250$ instead of $\eta_2=0.15$ and $\delta_c=150$) and threshold parameter
570 $\kappa_0=7\times 10^{-5}$ (instead of $\kappa_0=9\times 10^{-5}$). The remaining material constants (listed in Section 4) had a smaller
571 impact and were kept constant. In addition, one calculation was also performed for the case when elasto-
572 plasticity and damage were both switched off under compression. The decreasing parameter β
573 corresponded to a slight increase of the tensile fracture energy (from $G_f=100$ N/m up to $G_f=120$ N/m).
574 The increasing parameters η_2 and δ_c were equivalent to the decrease of the compressive strength and
575 compressive fracture energy (from $f_c=60$ MPa and $G_c=4000$ N/m down to $f_c=50$ MPa and $G_c=3000$ N/m).
576 The reduction of the threshold parameter κ_0 corresponded to the lower tensile strength and tensile fracture
577 energy (from $f_t=3.2$ MPa and $G_f=100$ N/m down to $f_t=2.6$ MPa and $G_f=80$ N/m).

578

579 The impact of the tensile strength and tensile fracture energy was more pronounced for the beam
0 S1D36a108 ($\eta_a=3$ with the diagonal tensile failure mode) than for S1D72a108 ($\eta_a=1.5$). In contrast, the
1 impacts of the compressive strength and fracture energy were most significant for the beam S1D72a108
2 ($\eta_a=1.5$ with the shear compression failure mode).

3

584 For the low beam S1D36a108 ($\eta_a=3$), the maximum vertical force became larger with increasing tensile
585 fracture energy and became smaller with decreasing compressive strength and fracture energy (Fig.19).
586 The decreasing threshold parameter κ_0 (lower tensile strength and tensile fracture energy) lead obviously
587 to a pronounced decrease of the ultimate vertical force (about 15%). The distance of inclined localized
588 zones from the support increased with decreasing parameter β and increasing parameters η_2 and δ_c . In
589 addition the localized zones became steeper. For the smaller value of κ_0 (Fig.19d), the agreement between
590 the shape and location of the critical diagonal localized zone as compared to the experiment was better.
591 In addition, the bending localized zones were more developed in the central beam part (Fig.19d) and their
592 number increased with growing tensile fracture energy.

593

594 For the high beam S1D72a108 ($\eta_a=1.5$), the vertical force decreased by 20% with decreasing
595 compressive strength and fracture energy (due to increase of the compression softening parameters η_2
596 and δ_c) (Fig.20). The decreasing tension softening parameter β lead to the growth of the vertical force
597 merely by 1%. For the smaller value of κ_0 , the bending localized zones were more developed in the
598 central beam part (Fig.20d). The location of the critical diagonal localized zone was not affected by the
599 change of material parameters. This shows that the 3D effect should be taken into account in FE analysis
600 in order to obtain better agreement for the beams with $\eta_a=1-1.5$. When plasticity and damage were
601 switched off in compression, the different failure modes occurred (Figs.19e and 20e). The beams'
602 strength strongly increased. Both the beams failed due to plastic flexural mechanism that was expressed
603 by reinforcement yielding. A large number of more developed bending localized zones were observed in
604 the central beam portion. The curved shear localized zones did not occur. Since all stress limits for
605 concrete were switched off in compression, the beam strength mainly depended upon the amount of steel
606 reinforcement that was high ($\rho_L=1.4\%$). The maximum concrete stress in the beam upper central part was
607 strongly above the concrete compressive strength (e.g. 100 MPa for the beam S1D36a108). Thus, a huge
608 increase of the ultimate vertical force occurred. The consideration of non-linearity in the compressive
609 region counteracted a strong shortcoming of our constitutive model caused by an isotropic response in
610 cracking. Our model for concrete needs the non-linearity in compression to get a more realistic shear
1 crack response (and to improve the incorrect physics of the model).

2

3

5.2 Effect of bond-slip stiffness

4

615 In the calculations, the different slip values were assumed according to Fig.8: $\delta_1=0.5$ mm, $\delta_2=1.5$ mm,
616 $\delta_3=4.5$ mm (instead of the basis data: $\delta_1=1$ mm, $\delta_2=2$ mm, $\delta_3=5$ mm) in order to investigate the effect of
617 the bond stiffness (the first set of constants corresponds to a stiffer bond). In addition two extreme bonds
618 were considered: 1) very weak bond ($\delta_1=100$ mm, $\delta_2=200$ mm, $\delta_3=500$ mm) (Fig.8) and 2) perfect bond.
619 The calculation results in Figs. 21 and 22 are shown for two beams: S1D36a108 ($\eta_a=3$) and S2D36a72
620 ($\eta_a=2$).

621

622 The ultimate vertical force P_{max} increased by about 3% (beam S1D36a108) and 5% (beam S2D36a72)
623 with the stiffer bond (curves 'b' in Figs.21 and 22). The pattern of localized zones was very similar for
624 the beam independently of the bond stiffness for the beam S1D36a72 with $\eta_a=2$ (Fig.21). For the beam
625 S1D36a108 ($\eta_a=3$), the critical diagonal shear crack was moved more to the beam mid-region with the
626 larger bond stiffness (Fig.22). The perfect bond lead to the increase of the peak load P_{max} by about 5%
627 (beam S1D36a108) and 8% (beam S2D36a72). For both the beams more localized bending zones
628 occurred in the beam mid-region. In contrast the very weak bond contributed to the decrease of P_{max} by
629 14% for the beam S1D36a108 and 5% for the beam S2D36a72. For both the beams less localized zones
630 occurred (e.g. two localized zones merely occurred in the beam mid-region of S1D36a72).

631

632 **6. Conclusions**

633

634 The following basic conclusions can be derived from our FE analyses on the size effect in RC beams
635 without stirrups which were scaled along the height or length:

636

637 - The enhanced coupled elastic-plastic-damage formulation was capable to offer good agreement with
638 the laboratory experiments using the same set of material constants with respect to both the strength and
639 failure modes. The material constants were calibrated by accompanying standard laboratory tests. The
640 differences between numerical outcomes and experimental results with respect to the critical diagonal
641 crack location grew with decreasing η_a (the numerical critical diagonal localization zone was located too
642 far from the beam support and its inclination to the horizontal was too steep for $\eta_a=1-1.5$ as compared to
643 the experimental outcomes). These discrepancies were due to 3D mechanical experimental effects that
644 were not considered in 2D simulations.

645

646 - The mechanical behaviour observed in RC beams was very sensitive to the beam dimensions. The shear
647 strength and brittleness increased with increasing effective height and decreased with increasing shear
648 span-effective height ratio. The diagonal tension failure (wherein normal displacements were higher than
649 tangential displacements along the critical diagonal crack) and shear compression failure (wherein
650 normal displacements were smaller than tangential displacements along the critical diagonal crack in the
651 top region) were realistically reproduced in calculations.

652

653 - The numerical shear strength of RC beams became higher with increasing tensile and compressive
654 fracture energy, tensile and compressive strength and slip-bond stiffness. During the diagonal tension
655 failure, the effect of tensile parameters was stronger and during shear compression failure, the effect of
656 compressive parameters was more pronounced. The size effect was now related to the actual failure
657 mechanism represented by its respective strength and energy parameters.

658

659 **Acknowledgments**

660 The research works have been carried out within the project: “*Innovative ways and effective methods of*
661 *safety improvement and durability of buildings and transport infrastructure in the sustainable*
662 *development*” financed by the European Union (POIG.01.01.02-10-106/09-01) and within the project:
663 “*Experimental and numerical analysis of coupled deterministic-statistical size effect in brittle materials*”
664 financed by the National Science Centre NCN (UMO-2013/09/B/ST8/03598).

665

666 The numerical calculations were performed on supercomputers of the Academic Computer Centre in
667 Gdańsk TASK.

668

669 **References**

670 [1] Z.P. Bažant, J. Planas, *Fracture and size effect in concrete and other quasi-brittle materials*. CRC
671 Press LCC; 1989.

672 [2] A. Carpinteri, Decrease of apparent tensile and bending strength with specimen size: two different
3 explanations based on fracture mechanics, *Int. J. Solids Struct.* 25(4) (1989) 407-29.

4 [3] K. Duan, Z. Hu, Specimen boundary induced size effect on quasi-brittle fracture, *Strength Fract.*
5 *Complexity* 2(2) (2004) 47-68.

6 [4] Z.P. Bažant, S.D. Pang, M. Vorechovsky, S. Novak, Energetic-statistical size effect simulated by
7 S6FEM with stratified sampling and crack band model, *Int. J. for Numerical Methods in Engineering*
8 71(11) (2007) 1297-1320.

- 679 [5] J.C. Walraven, *The influence of depth on the shear strength of lightweight concrete beams without*
680 *shear reinforcement*, Stevin Laboratory Report No.5-78-4, Delft University of Technology, vol. 36
681 (1978).
- 682 [6] Z.P. Bažant, M.T. Kazemi, Size effect on diagonal shear failure of beams without stirrups, *ACI Struct*
683 *J* 88(3) (1991) 268-76.
- 684 [7] J.K. Kim, Y.D. Park, Shear strength of reinforced high-strength concrete beams without web
685 reinforcement, *Mag Concr Res* 46(166) (1994) 7-16.
- 686 [8] K.H. Tan, H.Y. Lu, Shear behaviour of large reinforced concrete deep beams and code comparisons,
687 *ACI Struct J* 96(5) (1999) 836-45.
- 688 [9] D. Angelakos, E.C. Bentz, M.P. Collins, Effect of concrete strength and minimum stirrups on shear
689 strength of large members, *ACI Struct J* 98(3) (2001) 290-300.
- 690 [10] K.H. Yang, H.S. Chung, H.C Eun, Shear characteristics of high-strength concrete deep beams
691 without shear reinforcements, *Eng Struct* 25(10) (2003) 1343-52.
- 692 [11] K.H. Reineck, D. Kuchma, K.A. Kim, S. Marx, Shear database for reinforced concrete members
693 without shear reinforcement, *ACI Struct J* 100(2) (2003).
- 694 [12] A. Lubell, T. Sherwood, E. Bentz, M. Collins, Safe shear design of large, wide beams, *Concr Int*
695 26(1) (2004) 66-78.
- 696 [13] K.H. Tan, G.H. Cheng, H.K. Cheong, Size effect in shear strength of large beams-behaviour and
697 finite element modelling, *Mag Concrete Res* 57(8) (2005) 497-509.
- 698 [14] E. Syroka-Korol, J. Tejchman, Experimental investigations of size effect in reinforced concrete
699 beams failing by shear. *Engineering Structures* 58 (2014) 63-78.
- 700 [15] J.C. Walraven, N. Lehwalter, Size effects in short beams loaded in shear, *ACI Struct J* 91(5) (1994)
701 585-93.
- 702 [16] N. Zhang, K.H. Tan, Size effect in RC deep beams: Experimental investigation and STM
703 verification, *Eng Struct* 29 (2007) 3241-54.
- 704 [17] C.M. Belgin, S. Şener, Size effect on failure of overreinforced concrete beams, *Eng Fract Mech*
705 75(8) (2008) 2308-19.
- 6 [18] C. Carpintieri, J.R Carmona, G. Ventura, Failure mode transitions in reinforced concrete beams. Part
7 2: Experimental tests, *ACI Struct J* 108 (2011) 286-93.
- 8 [19] M. Słowik, P. Smarzewski, Study of the scale effect on diagonal crack propagation in concrete
9 beams, *Comput Mater Sci* 64 (2012) 216-220.
- 0 [20] J. Suchorzewski, E. Korol, J. Tejchman, Z. Mroz, Experimental study of shear strength and failure
1 mechanisms in RC beams scaled along height or length, *Engineering Structures* 157 (2018) 203-223.

- 712 [21] ACI 318-14: Building code requirements for structural concrete, American Concrete Institute, 2014.
- 713 [22] N. Zhang, K. Tan, Direct strut-and-tie model for single span and continuous deep beams, *Eng.*
714 *Structures* 29 (2007) 2987-3001.
- 715 [23] D. Krajcinovic, G. Fonseka, The continuous damage theory of brittle materials, *Journal of Applied*
716 *Mechanics ASME* 48 (4) (1981) 809-824.
- 717 [24] J. Mazars, A description of micro- and macroscale damage of concrete structures, *Engineering*
718 *Fracture Mechanics* 25(5-6) (1986) 729-737.
- 719 [25] J.C. Simo, J. Ju, Strain- and stress-based continuum damage models, *International Journal for Solids*
720 *and Structures* 23(7) (1987) 821-840.
- 721 [26] J. Lubliner, J. Oliver, S.E. Oller, E. Onate, A plastic-damage model for concrete, *International Jour-*
722 *nal of Solids and Structures*, 25(3) (1989) 299-326.
- 723 [27] G. Meschke, R. Lackner, H.A. Mang, An anisotropic elastoplastic-damage model for plain concrete,
724 *Int. J. for Numerical Methods in Engineering* 42(4) (1998) 702-727.
- 725 [28] R. Faria, J. Oliver, M. Cervera, A strain-based plastic viscous-damage model for massive concrete
726 structures, *International Journal of Solids and Structures* 35(14) (1998) 1533-1558.
- 727 [29] E. Hansen, K. Willam, A two-surface anisotropic damage-plasticity model for plane concrete, *Pro-*
728 *ceedings Int. Conf. Fracture Mechanics of Concrete Materials*, R. de Borst [Ed.], Paris, Balkema, 549-
729 556, 2001.
- 730 [30] J.F. Chen, E.V. Morozov, K. Shankar, A combined elastoplastic damage model for progressive fail-
731 ure analysis of composite materials and structures, *Composite Structures* 94 (2012) 3478-3489.
- 732 [31] P. Grassl, D. Xenos, U. Nyström, R. Rempling, K. Gylltoft, CDPM2: A damage-plasticity approach
733 to modelling the failure of concrete. *International Journal of Solids and Structures*, 50 (2013) 3805-
734 3816.
- 735 [32] J. Mihai, A. Jefferson, L. Lyons, Plastic-damage constitutive model for the finite element analysis
736 of fibre reinforced concrete, *Engineering Fracture Mechanics* 159 (2016) 35-62.
- 737 [33] G. Xotta, S. Beizaee, K.J. Willam, Bifurcation investigations of coupled damage-plasticity models
738 for concrete materials, *Computer Methods in Applied Mechanics and Engineering* 298 (2016) 428-452.
- 9 [34] E. Korol, J. Tejchman, Z. Mroz, Experimental and numerical assessment of size effect in
0 geometrically similar slender concrete beams with basalt reinforcement, *Engineering Structures* 141
1 (2017) 272-291.
- 2 [35] I. Marzec, L. Skarżyński, J. Bobiński, J. Tejchman, Modelling reinforced concrete beams under
3 mixed shear-tension failure with different continuous FE approaches, *Computers and Concrete* 12(5)
4 (2013) 585-612.

- 745 [36] L. Skarżyński, I. Marzec, J. Tejchman, Experiments and numerical analyses for composite RC-EPS
746 slabs, *Computers and Concrete* 20(6) (2017) 689-704.
- 747 [37] I. Marzec, J. Tejchman, Enhanced coupled elasto-plastic-damage models to describe concrete
748 behaviour in cyclic laboratory tests: comparison and improvement, *Archives of Mechanics* 64(3) (2012)
749 227-259.
- 750 [38] I. Marzec, J. Tejchman, Computational modelling of concrete behaviour under static and dynamic
751 conditions, *Bulletin of the Polish Academy of Sciences - Technical Sciences* 61(1) (2013) 85-96.
- 752 [39] I. Marzec, J. Tejchman, A. Winnicki, Computational simulations of concrete behaviour under
753 dynamic conditions using elasto-visco-plastic model with non-local softening, *Computers and Concrete*
754 15(4) (2015) 515-545.
- 755 [40] J. Pamin, R. de Borst, Stiffness degradation in gradient-dependent coupled damage-plasticity.
756 *Archives of Mechanics* 51, 3-4 (1999) 419-446.
- 757 [41] T. Majewski, J. Bobinski, J. Tejchman, FE-analysis of failure behaviour of reinforced concrete col-
758 umns under eccentric compression, *Engineering Structures* 30(2) (2008) 300-317.
- 759 [42] T. Malecki, T. Marzec, J. Bobiński, J. Tejchman, Effect of a characteristic length on crack spacing
760 in a reinforced concrete bar under tension, *Mechanics Research Communications* 34(5-6) (2007) 460-
761 465.
- 762 [43] Abaqus documentation, Version 6.13; 2013.
- 763 [44] R.H.J. Peerlings, R. de Borst, W.A.M. Brekelmans, M.G.D., Geers, Gradient enhanced damage
764 modelling of concrete fracture. *Mechanics of Cohesive-Frictional Materials* 3 (1998) 323-342.
- 765 [45] M.G.D. Geers, Experimental analysis and computational modeling of damage and fracture, *PhD*
766 *Thesis*, Eindhoven University of Technology, 1997.
- 767 [46] J. Lee, G.L. Fenves, Plastic-damage model for cyclic loading of concrete structures. *Journal of*
768 *Engineering Mechanics* 124(8) (1998) 892-900.
- 769 [47] I. Carol, K. Willam, Spurious energy dissipation/generation in stiffness recovery models for elastic
770 degradation and damage, *International Journal Solids Structures*, 33(20-22), (1996) 2939-2957.
- 771 [48] D. Karsan, J. O. Jirsa, Behavior of concrete under compressive loadings, *J. Struct. Div. ASCE* 95(12)
2 (1969) 2543-2563.
- 3 [49] D. A. Hordijk, Local approach to fatigue of concrete, *PhD Thesis*, Delft University of Technology,
4 1991.
- 5 [50] G. Pijauder-Cabot, Z.P. Bažant, Non-local damage theory, *ASCE Journal of Engineering Mechanics*
6 113 (1987) 1512-1533.

- 777 [51] Z.P. Bažant, M. Jirásek, Non-local integral formulations of plasticity and damage: survey of
778 progress, *Journal of Engineering Mechanics* 128 (2002) 1119-1149.
- 779 [52] J. Bobiński, J. Tejchman, Numerical simulations of localization of deformation in quasi-brittle
780 materials within non-local softening plasticity, *Computers and Concrete* 1(4) (2004) 1-22.
- 781 [53] J. Bobiński, J. Tejchman, Comparison of continuous and discontinuous constitutive models to
782 simulate concrete behaviour under mixed mode failure conditions, *Int. J. Num. Anal. Meths Geom.* 40
783 (2016) 406-435.
- 784 [54] G. Borino, B. Failla, F. Parrinello, A symmetric formulation for non-local damage models, In Mang
785 HA, Rammerstorfer FG, Eberhardsteiner J. (eds). *Proc. of 5th World Congress on Computational*
786 *Mechanics* (WCCM V), Vienna, Austria, 2002. Vienna University of Technology. ISBN 3-9501554-0-6,
787 <http://wccm.tuwien.ac.at>.
- 788 [55] P. Grassl, D. Xenos, M. Jirásek, M. Horák, Evaluation of nonlocal approaches for modelling fracture
789 near nonconvex boundaries. *Int. J. Solids Struct.*, 51 (2014) 3239-51.
- 790 [56] P. Havlásek P., Grassl, M. Jirásek, Analysis of size effect on strength of quasi-brittle materials using
791 integral-type nonlocal models, *Engineering Fracture Mechanics* (2016) 72–85.
- 792 [57] J. Tejchman, J. Bobiński, *Continuous and discontinuous modeling of fracture in concrete using*
793 *FEM*. Springer, Berlin-Heidelberg (eds. W. Wu and R. I. Borja), 2013.
- 794 [58] D. Xenos, P. Grassl, Modelling the failure of reinforced concrete with nonlocal and crack band
795 approaches using the damage-plasticity model CDPM. *Finite Elements in Analysis and Design* 117-118
796 (2016) 11-20.
- 797 [59] R. Mahnken, E. Kuhl. Parameter identification of gradient enhanced damage models, *European*
798 *Journal of Mechanics A/Solids*, 18 (1999) 819-835.
- 799 [60] L. Skarżyński, E. Syroka, J. Tejchman, Measurements and calculations of the width of fracture
800 process zones on the surface of notched concrete beams, *Strain* 47 (2011) 319-332.
- 801 [61] L. Skarżyński, J. Tejchman, Experimental investigations of fracture process in plain and reinforced
802 concrete beams under bending, *Strain* 49, 6 (2013) 521-543.
- 803 [62] E. Syroka, J. Bobiński, J. Tejchman, FE analysis of reinforced concrete corbels with enhanced con-
4 tinuum models. *Finite Element Methods in Analysis and Design* 47, 9 (2011) 1066-1078.
- 5 [63] CEB-FIP, CEB-FIP model code 1990, 1993.
- 6 [64] S. Yang, Y. Chen, D. Du, G. Fan, Determination of boundary effect on shear fracture energy at steel
7 bar–concrete interface. *Engineering Fracture Mechanics* 153 (2016) 319-330.
- 8 [65] E. Syroka-Korol, J. Tejchman, Experimental investigations of size effect in reinforced concrete
9 beams failing by shear. *Eng Struct* 58 (2014) 63-78.

810 [66] E. Korol, J. Tejchman, Z. Mróz, FE analysis of size effects in reinforced concrete beams without
811 shear reinforcement based on stochastic elasto-plasticity with non-local softening, *Finite Elements in*
812 *Analysis and Design* 1 (2014) 25-41.

813

814

815

816

LIST OF FIGURES

817

818

819 **Fig.1:** Experimental reinforced concrete beams under four-point bending: A) loading scheme for series
820 '1', B) loading scheme for series '2' and C) cross-section of: a) beam S1D18a108, b) beams: S1D36a108,
821 S2D36a36, S2D36a72, S2D36a108 and c) beam S1D72a108 [20]

822

823 **Fig.2:** Crack pattern at failure typical for each beam geometry depending upon ratio a/D for different
824 failure mode: a) reinforcement yielding ($\eta_a=6$), b) shear failure mode in concrete (diagonal tension) with
825 ($\eta_a=3$), c) shear failure in concrete (diagonal shear-compression) ($\eta_a=1.5$), d) shear failure in concrete
826 (diagonal tension) ($\eta_a=2$), e) shear failure in concrete (diagonal shear-compression) ($\eta_a=2$) and f) shear
827 failure in concrete (diagonal shear-compression) ($\eta_a=1$) (critical diagonal crack marked in red, beams
828 are not proportionally scaled) [20]

829

830 **Fig.3:** Failure surface of coupled Drucker-Prager-Rankine criterion for concrete in space of principal
831 stresses

832

833 **Fig.4:** Uniaxial response (stress-strain curve) of coupled elasto-plastic-damage model under cyclic
834 loading: a) stiffness recovery concept with different damage scale factors a_t and a_c , b) influence of
835 different damage splitting factors a_t and a_c and c) influence of load sequence (tension/compression and
836 compression/tension) with damage splitting factors $a_t=0.2$ and $a_c=0.8$)

837

838 **Fig.5:** Response of coupled elasto-plastic-damage model during uniaxial cyclic tests as compared with
839 experimental data: a) for concrete specimen under uniaxial cyclic compression (experimental stress-
840 strain curve by Karsan and Jirsa [48]) and b) for concrete beam under four-point cyclic bending under
841 tensile failure (experimental force-displacement curve by Hordijk [49]) [37]

842

3 **Fig.6:** Effect of different material constants on uniaxial response of coupled elasto-plastic-damage model
4 under: A) cyclic uniaxial compression and B) cyclic uniaxial tension

5

6 **Fig.7:** Stress-strain curves for concrete from element tests using elasto-plastic-damage model: a) cyclic
7 uniaxial compression, b) cyclic uniaxial tension and c) cyclic simple shear

8

849 **Fig.8:** Bond stress-slip relationship $\tau_b=f(\delta)$ by CEB-FIP [63] (Eq.17) with different parameters δ_i

850

851 **Fig.9:** Boundary conditions and FE mesh for RC beams (diameter of small yellow circle is related to
852 characteristic length l_c and diameter of larger yellow circle is related to influence range of non-locality
853 $3l_c$)

854

855 **Fig.10:** Experimental and calculated force-deflection $F=f(u)$ diagrams for beams: a) S1D18a108 ($D=180$
856 mm, $L_{eff}=2700$ mm, $a=1080$ mm, $\eta_l=15$, $\eta_a=6$), b) S1D36a108 and S2D36a108 ($D=360$ mm,
857 $L_{eff}=2700$ mm, $a=1080$ mm, $\eta_l=7.5$, $\eta_a=3$), c) S1D72a108 ($D=720$ mm, $L_{eff}=2700$ mm, $a=1080$ mm,
858 $\eta_l=3.75$, $\eta_a=1.5$), d) S2D36a36 ($D=360$ mm, $L_{eff}=1260$ mm, $a=360$ mm, $\eta_l=3.75$, $\eta_a=1$) and e)
859 S2D36a72 ($D=360$ mm, $L_{eff}=1980$ mm, $a=720$ mm, $\eta_l=5.5$, $\eta_a=2$)

860

861 **Fig.11:** Shear strength τ_c from experiments, calculations and Eq.18: a) for varying shear span parameter
862 $\eta_a=a/D$ and b) for varying length parameter $\eta_l=l_{eff}/D$ (note that beams S1D18a108 for $\eta_a=6$ failed in
863 flexural mechanism)

864

865 **Fig.12:** Contours of non-local equivalent strain measure $\bar{\epsilon}$ with attached scale as compared with
866 experimental cracks pattern for beams of series I ($L_{eff}=2700$ mm): a) S1D18a108 ($D=180$ mm,
867 $a=1080$ mm, $\eta_l=15$, $\eta_a=6$), b) S1D36a108 ($D=360$ mm, $a=1080$ mm, $\eta_l=7.5$, $\eta_a=3$) and c) S1D72a108
868 ($D=720$ mm, $a=1080$ mm, $\eta_l=3.75$, $\eta_a=1.5$) (experimental critical diagonal crack is marked by red arrow,
869 numerical critical localization zone is marked by yellow arrow, note that beams are not proportionally
870 scaled and steel bars are not shown)

871

872 **Fig.13:** Contours of non-local equivalent strain measure $\bar{\epsilon}$ with attached scale as compared with
873 experimental cracks pattern for beams ($D=360$ mm): a) S2D36a72_1 and b) S2D36a72_2 ($L_{eff}=1980$ mm,
874 $a=720$ mm, $\eta_l=5.5$, $\eta_a=2$) and c) S2D36a36 ($L_{eff}=1260$ mm, $a=360$ mm, $\eta_l=3.75$, $\eta_a=1$) (experimental
875 critical diagonal crack is marked by red arrow, numerical critical diagonal localization zone is marked
6 by yellow arrow, note that beams are not proportionally scaled and steel bars are not shown)

7

8 **Fig.14:** Diagonal failure crack/localized zone inclination ϕ to horizontal in RC beams for experimental
9 series '1' (S1, square markers) and '2' (S2, triangle markers) versus ratio η_a as compared with FEM

0



881 **Fig.15:** Experimental and calculated normalized height of compressive zone above shear and bending
882 crack/localized zone for varying shear span parameter $\eta_a=a/D$ (S1 - experimental series '1', S2 -
883 experimental series '2', note that beams for $\eta_a=6$ failed in flexural mechanism)

884

885 **Fig.16:** Calculated evolution of normal and tangential displacements at critical diagonal localization zone
886 from FEM for beam S1D36a108 ($\eta_a=3$) as compared to experiments: a) locations (marked by yellow
887 arrows) and b) vertical force versus displacements: ω - normal displacement, δ - tangential displacement
888 (experimental critical diagonal crack is marked by red arrow)

889

890 **Fig.17:** Calculated evolution of normal and tangential displacements at critical diagonal localization zone
891 from FEM for beam S1D72a108 ($\eta_a=1.5$) as compared to experiments: a) locations (marked by yellow
892 arrows) and b) vertical force versus displacements: ω - normal displacement, δ - tangential displacement
893 (experimental critical diagonal crack is marked by red arrow)

894

895 **Fig.18:** Comparison between calculated (left side) and experimental (right side) normal displacements ω
896 along normalized critical diagonal crack/localization zone length l_{exp}/l_{FEM} for: a) beam S1D36a108 and
897 b) beam S1D72a108 (horizontal coordinate 0 - point above reinforcement (point '1' in Figs.16 and 17)
898 and horizontal coordinate 1 - point in upper beam region (point '3' in Figs.16 and 17)).

899

900 **Fig.19:** Calculated force-deflection curves and distributions of non-local equivalent strain measure from
901 FE analyses using coupled elasto-plastic-damage with non-local softening as compared to experiments
902 (beam S1D36a108, $\eta_a=3$): a) with basis set of material constants in Section 4, b) with softening constant
903 $\beta=60$ (instead of $\beta=85$), c) with softening constants $\eta_2=0.20$ and $\delta_c=250$ (instead of $\eta_2=0.15$ and $\delta_c=150$)
904 d) with $\kappa_0=7 \times 10^{-5}$ (instead of $\kappa_0=9 \times 10^{-5}$) and e) without plasticity and damage under compression

905

906 **Fig.20:** Calculated force-deflection curves and distributions of non-local equivalent strain measure from
907 FE analyses using coupled elasto-plastic-damage with non-local softening as compared to experiments
8 (beam S1D72a108, $\eta_a=1.5$): a) with basis set of material constants in Section 4, b) with softening constant
9 $\beta=60$ (instead of $\beta=85$), c) with softening constants $\eta_2=0.20$ and $\delta_c=250$ (instead of $\eta_2=0.15$ and $\delta_c=150$),
0 d) with $\kappa_0=7 \times 10^{-5}$ (instead of $\kappa_0=9 \times 10^{-5}$) and e) without plasticity and damage under compression

1



912 **Fig.21:** Calculated force-deflection curves (dotted line - experiments) and distributions of non-local
913 equivalent strain measure from FE analyses using coupled elasto-plastic-damage with non-local
914 softening as compared to experiments (beam S2D36a72, $\eta_a=2$) for bond-slip model of Fig.8: a) Eq.17
915 with $\delta_1=1$ mm, $\delta_2=2$ mm, and $\delta_3=5$ mm (basic data), b) Eq.17 with $\delta_1=0.5$ mm, $\delta_2=1.5$ mm and
916 $\delta_3=4.5$ mm, c) Eq.17 with $\delta_1=100$ mm, $\delta_2=200$ mm and $\delta_3=500$ mm and d) perfect bond model
917

918 **Fig.22:** Calculated force-deflection curves (dotted line - experiments) and distributions of non-local
919 equivalent strain measure from FE analyses using coupled elasto-plastic-damage with non-local
920 softening as compared to experiments (beam S1D36a108, $\eta_a=3$) for bond-slip model of Fig.8: a) Eq.17
921 with $\delta_1=1$ mm, $\delta_2=2$ mm, and $\delta_3=5$ mm (basic data), b) Eq.17 with $\delta_1=0.5$ mm, $\delta_2=1.5$ mm and
922 $\delta_3=4.5$ mm, c) Eq.17 with $\delta_1=100$ mm, $\delta_2=200$ mm and $\delta_3=500$ mm and d) perfect bond model
923
924
925
926
927
928
929
930
931
932
933
934
935
936
937
938



LIST OF FIGURES

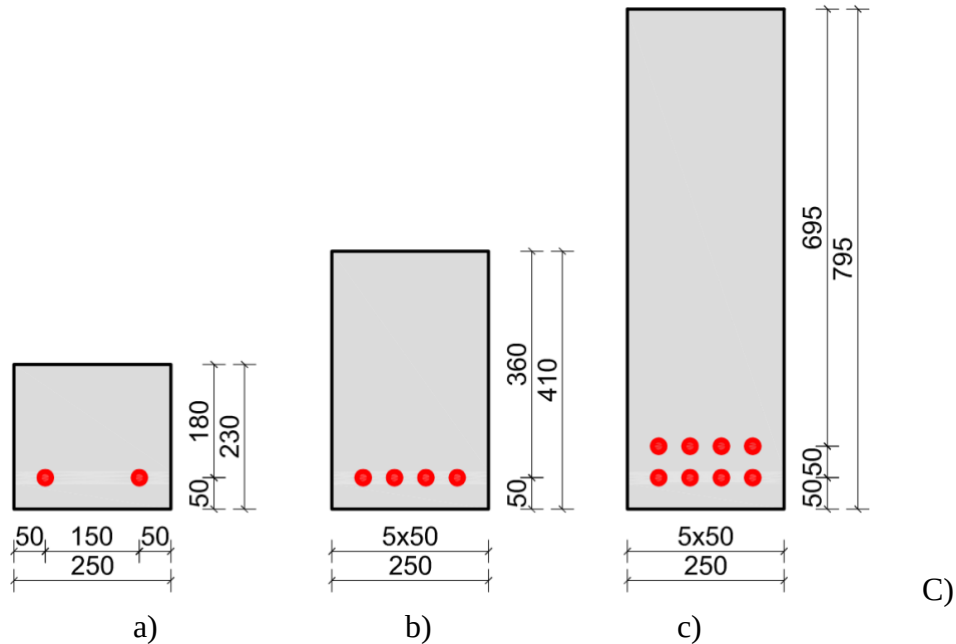
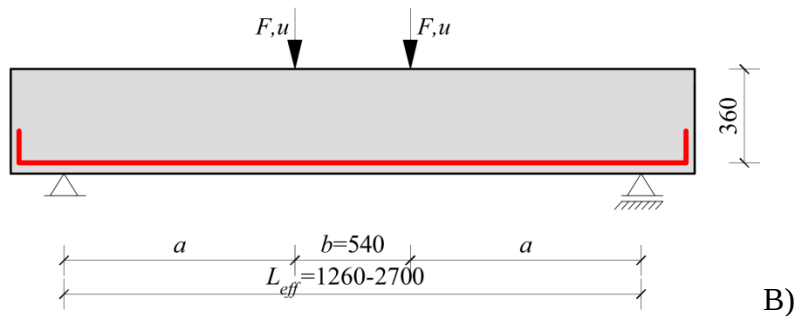
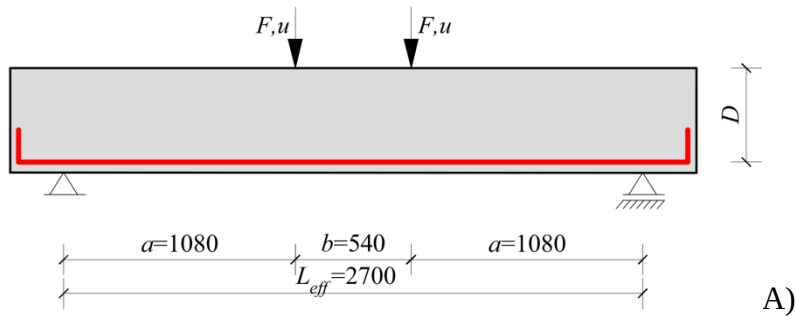


Fig.1: Experimental reinforced concrete beams under four-point bending: A) loading scheme for series '1', B) loading scheme for series '2' and C) cross-section of: a) beam S1D18a108, b) beams: S1D36a108, S2D36a36, S2D36a72, S2D36a108 and c) beam S1D72a108 [20]

FIGURE 1

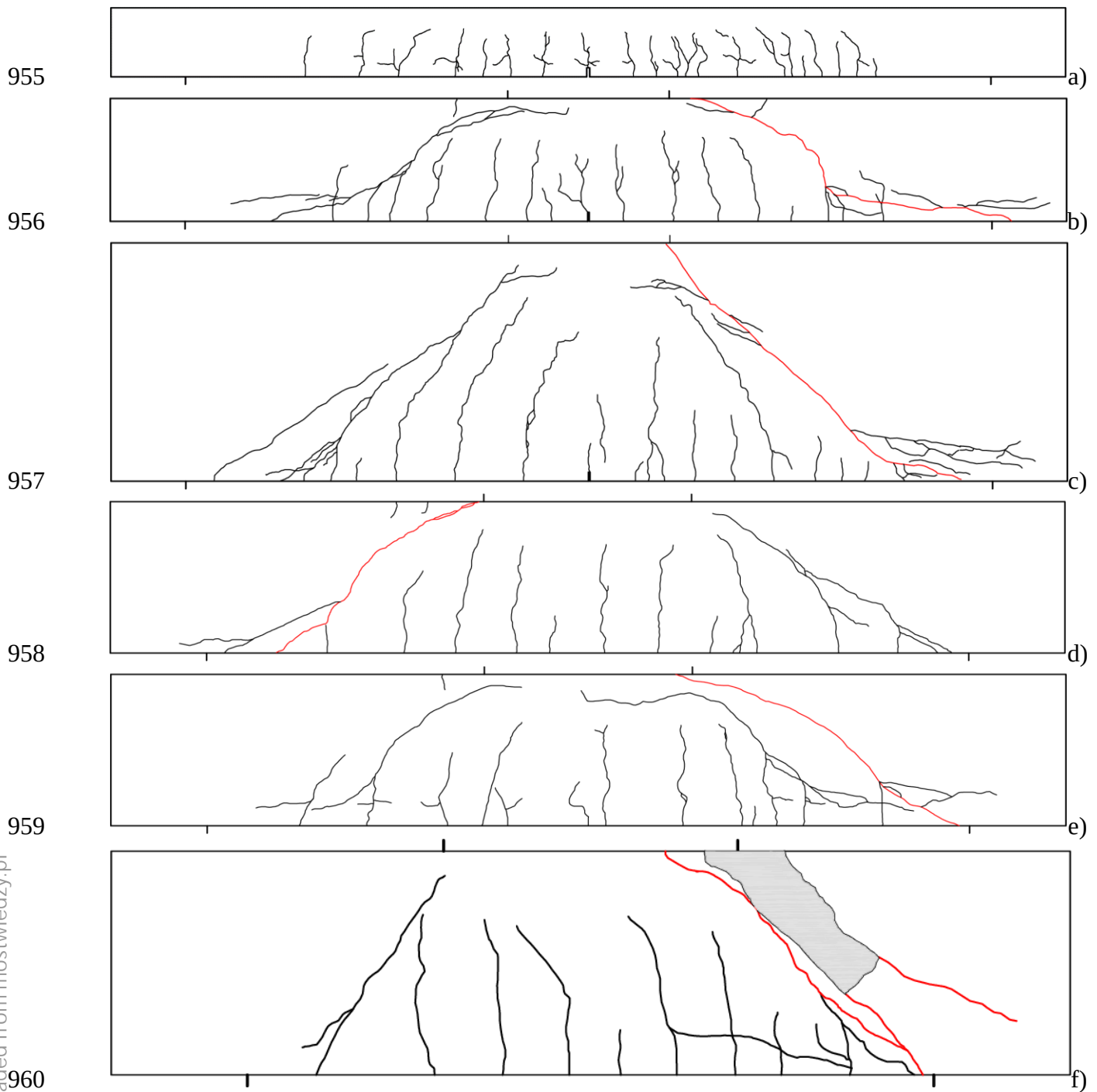


Fig.2: Crack pattern at failure typical for each beam geometry depending upon ratio a/D for different failure mode: a) reinforcement yielding ($\eta_a=6$), b) shear failure mode in concrete (diagonal tension) with ($\eta_a=3$), c) shear failure in concrete (diagonal shear-compression) ($\eta_a=1.5$), d) shear failure in concrete (diagonal tension) ($\eta_a=2$), e) shear failure in concrete (diagonal shear-compression) ($\eta_a=2$) and f) shear failure in concrete (diagonal shear-compression) ($\eta_a=1$) (critical diagonal crack marked in red, beams are not proportionally scaled) [20]

FIGURE 2

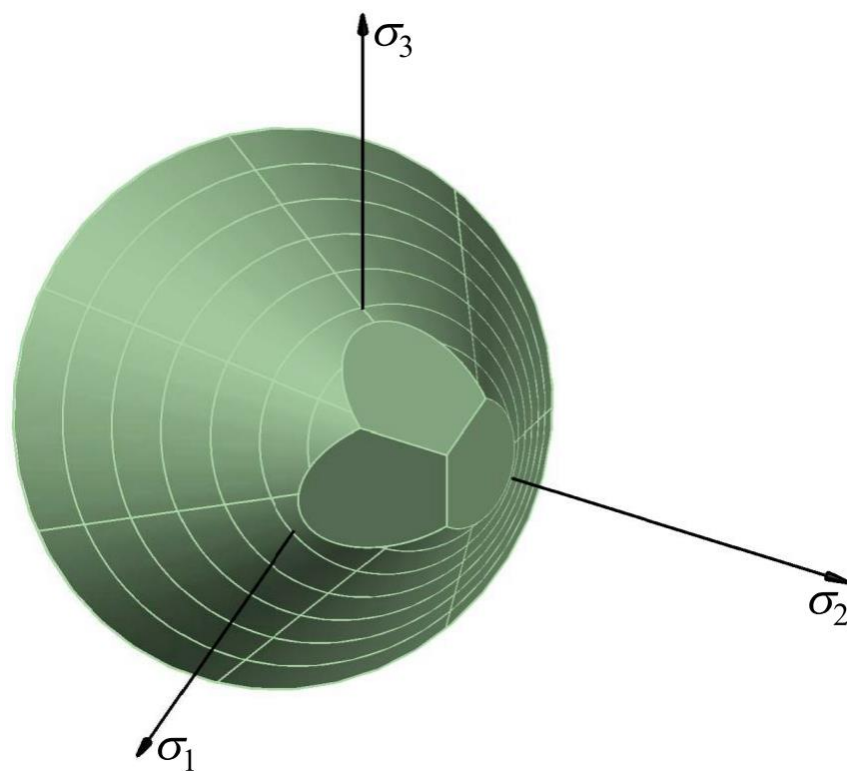


Fig.3: Failure surface of coupled Drucker-Prager-Rankine criterion for concrete in space of principal stresses

FIGURE 3

969
970
971
972
973
974
975
976
977
978
979

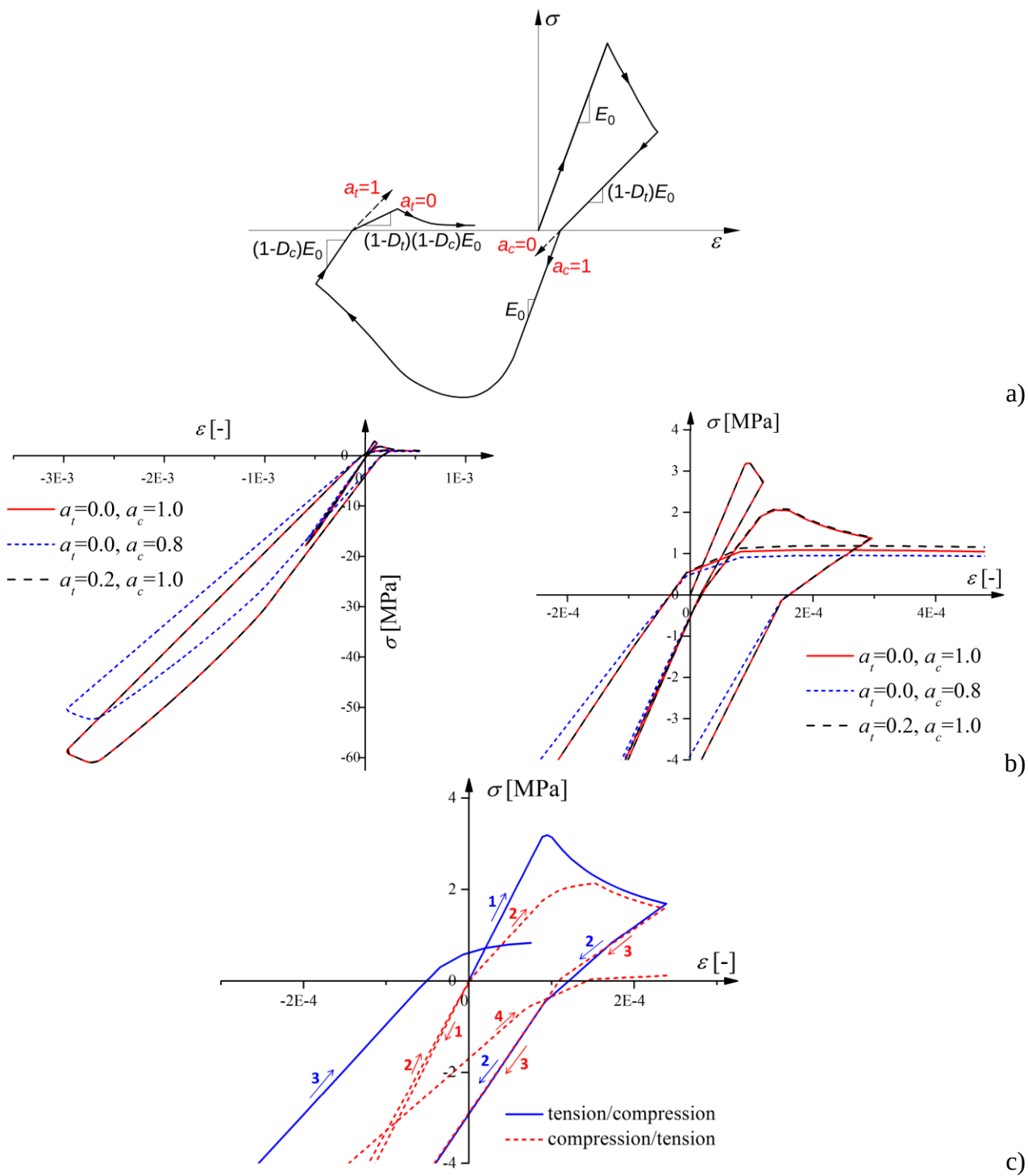


Fig.4: Uniaxial response (stress-strain σ - ϵ curve) of coupled elasto-plastic-damage model under cyclic loading: a) stiffness recovery concept with different damage scale factors a_t and a_c , b) influence of different damage splitting factors a_t and a_c and c) influence of load sequence (tension/compression or compression/tension) with damage splitting factors $a_t=0.2$ and $a_c=0.8$)

FIGURE 4

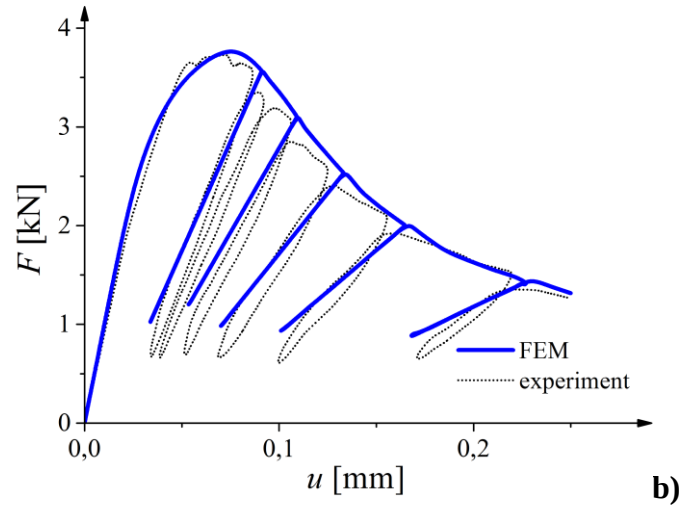
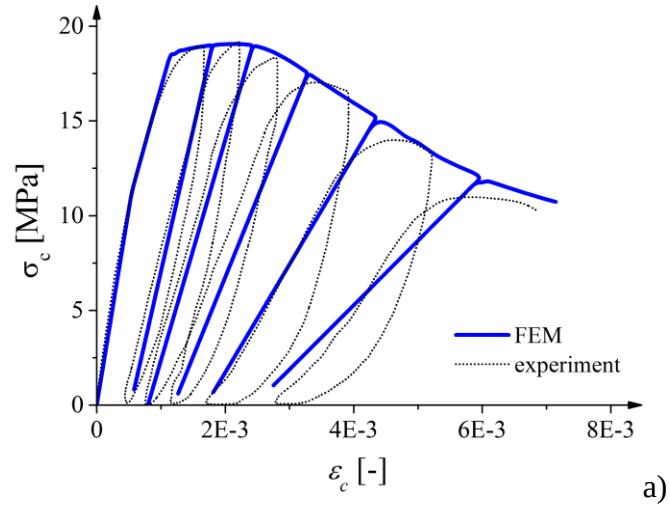
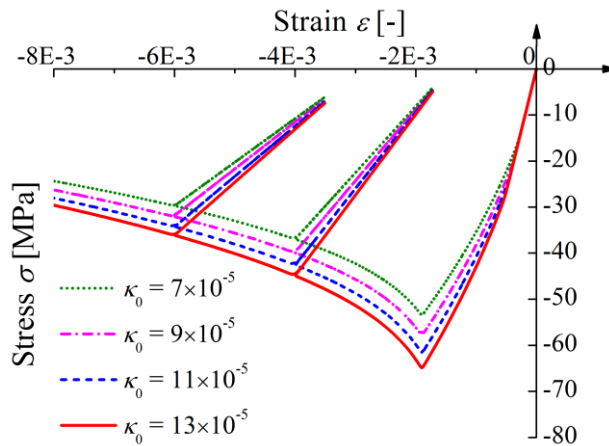
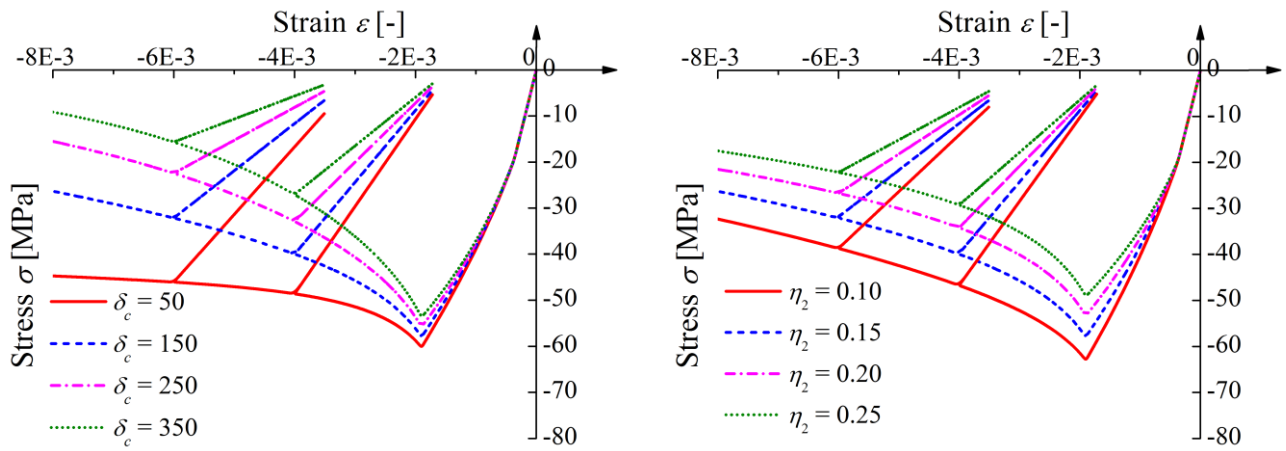
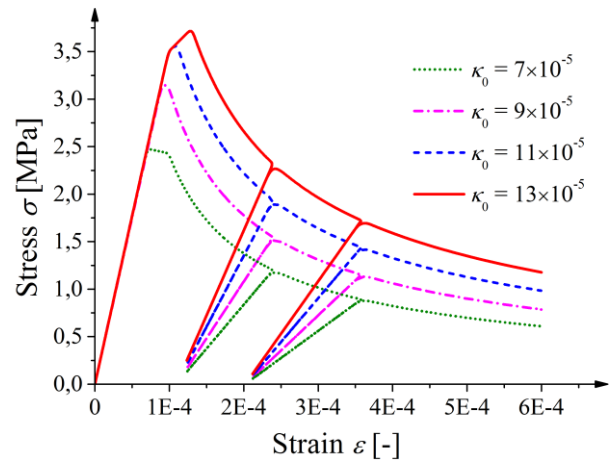
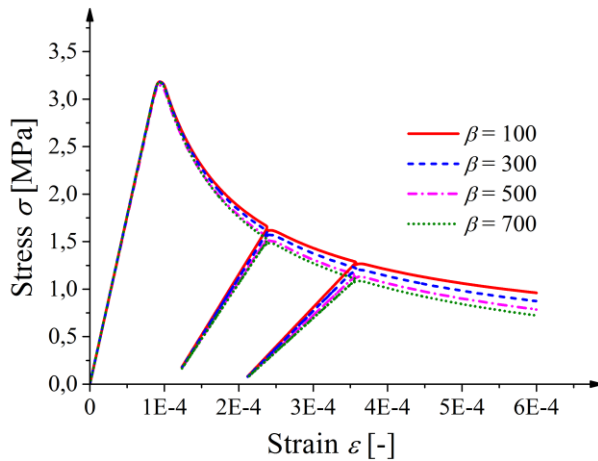


Fig.5: Response of coupled elasto-plastic-damage model during uniaxial cyclic tests as compared with experimental data: a) for concrete specimen under uniaxial cyclic compression (experimental stress-strain curve by Karsan and Jirsa [48]) and b) for concrete beam under four-point cyclic bending under tensile failure (experimental force-displacement curve by Hordijk [49]) [37]

FIGURE 5



A)

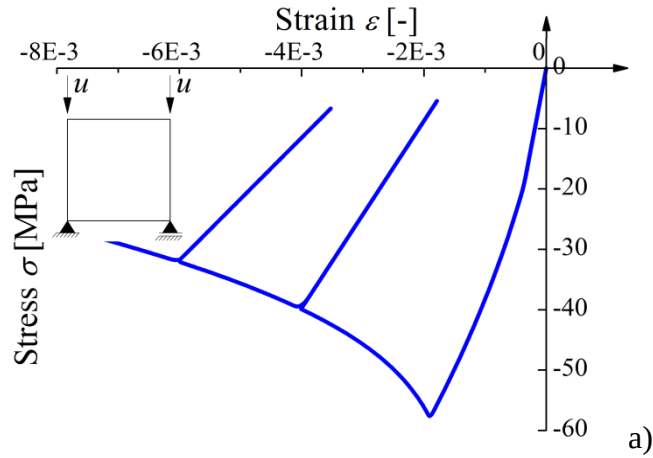


B)

Fig.6: Effect of different material constants on uniaxial cyclic response of coupled elasto-plastic-damage model under: A) cyclic uniaxial compression and B) cyclic uniaxial tension

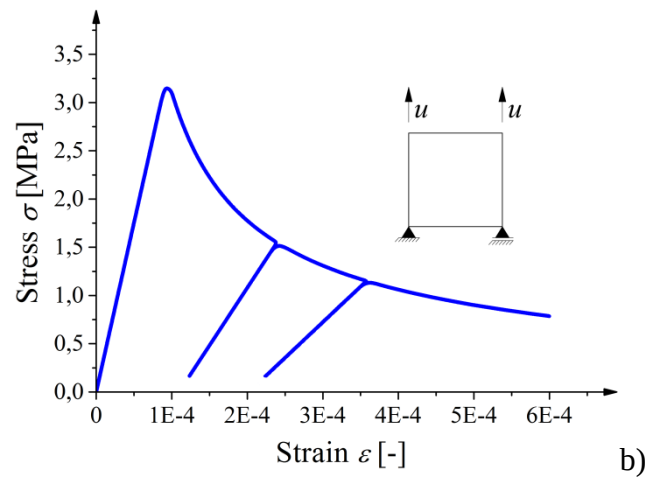
FIGURE 6

1004



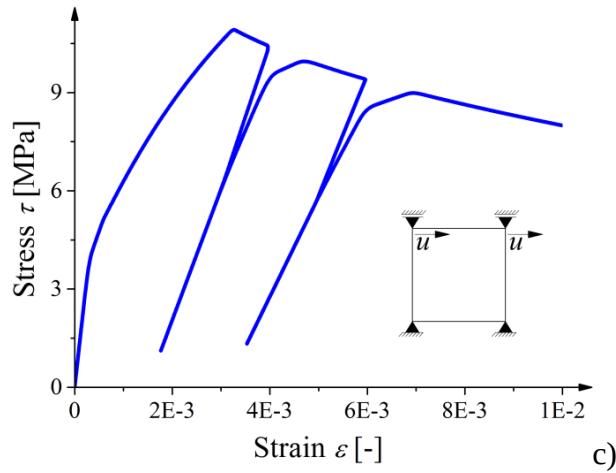
1005

1006



1007

1008

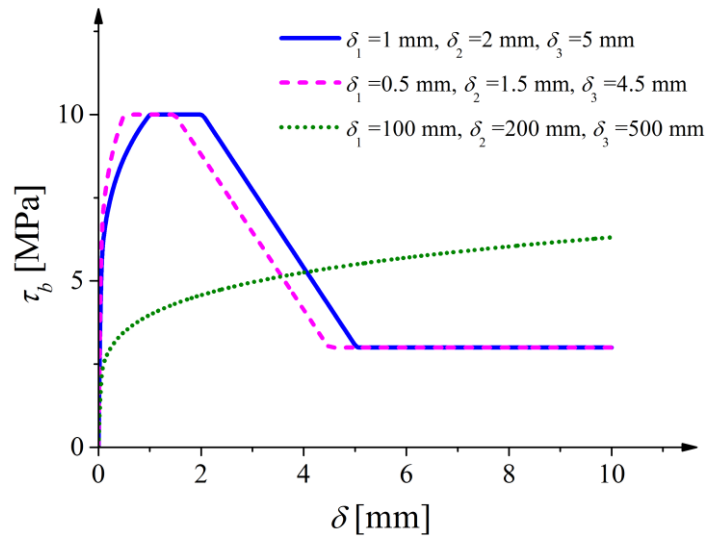


1009

Fig.7: Stress-strain curves for concrete from element tests using elasto-plastic-damage model: a) cyclic uniaxial compression, b) cyclic uniaxial tension and c) cyclic simple shear

FIGURE 7

1014
1015
1016
1017
1018

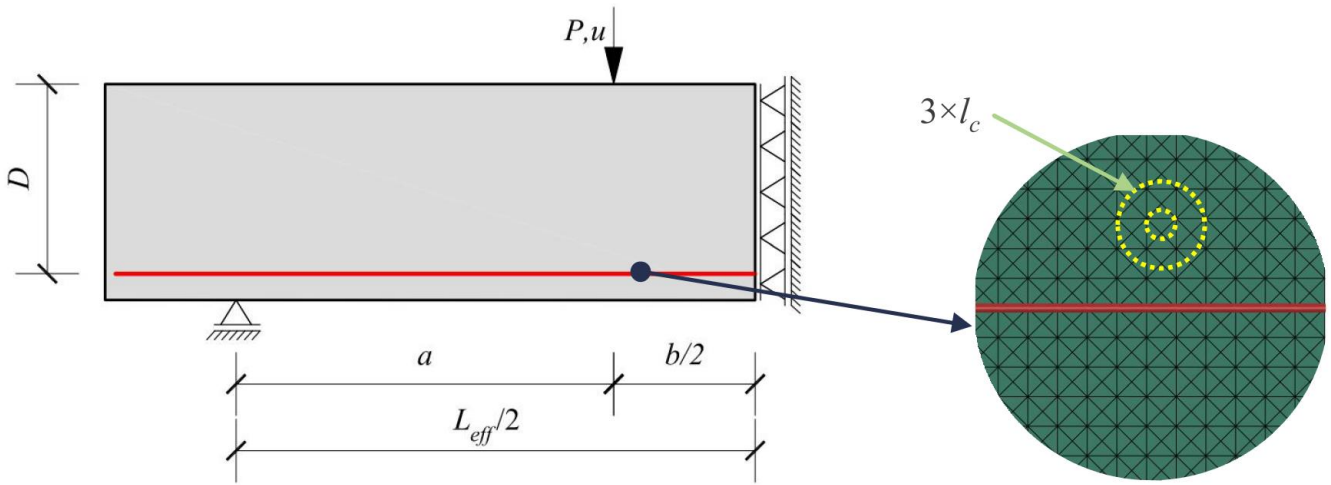


1019
1020
1021
1022
1023
1024
1025
1026
1027
1028
1029

Fig.8: Bond stress-slip relationship $\tau_b=f(\delta)$ by CEB-FIP [63] (Eq.17) with different parameters δ_i

FIGURE 8

1030
1031
1032
1033
1034



1035
1036
1037
1038
1039
1040
1041
1042
1043
1044

Fig.9: Boundary conditions and FE mesh for RC beams (diameter of small yellow circle is related to characteristic length l_c and diameter of larger yellow circle is related to influence range of non-locality $3l_c$)

1045
1046

FIGURE 9

1047
1048
1049
1050
1051
1052
1053

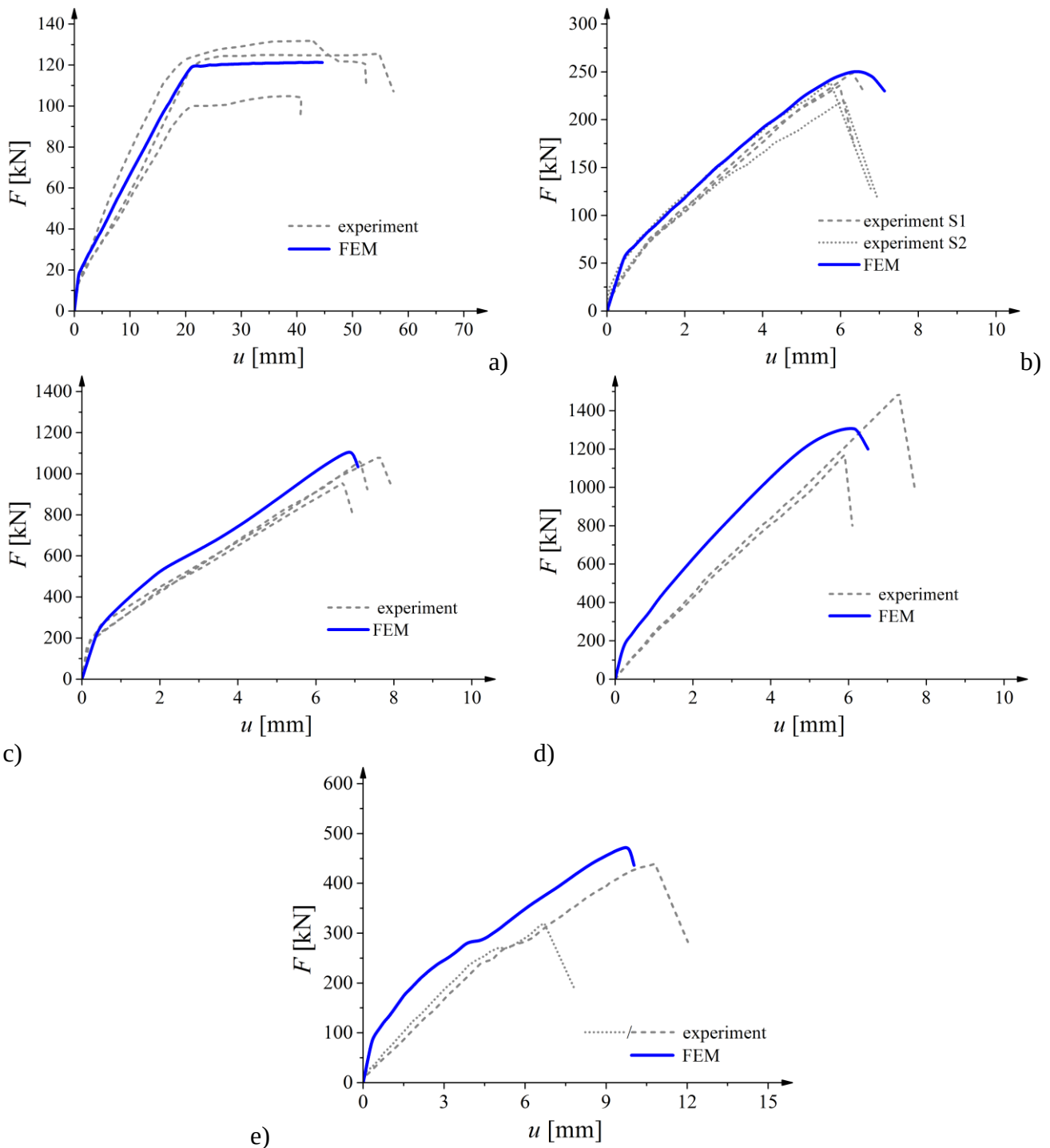


Fig.10: Experimental and calculated force-deflection $F=f(u)$ diagrams for beams: a) S1D18a108 ($D=180$ mm, $L_{eff}=2700$ mm, $a=1080$ mm, $\eta_l=15$, $\eta_a=6$), b) S1D36a108 and S2D36a108 ($D=360$ mm, $L_{eff}=2700$ mm, $a=1080$ mm, $\eta_l=7.5$, $\eta_a=3$), c) S1D72a108 ($D=720$ mm, $L_{eff}=2700$ mm, $a=1080$ mm, $\eta_l=3.75$, $\eta_a=1.5$), d) S2D36a36 ($D=360$ mm, $L_{eff}=1260$ mm, $a=360$ mm, $\eta_l=3.75$, $\eta_a=1$) and e) S2D36a72 ($D=360$ mm, $L_{eff}=1980$ mm, $a=720$ mm, $\eta_l=5.5$, $\eta_a=2$)

FIGURE 10

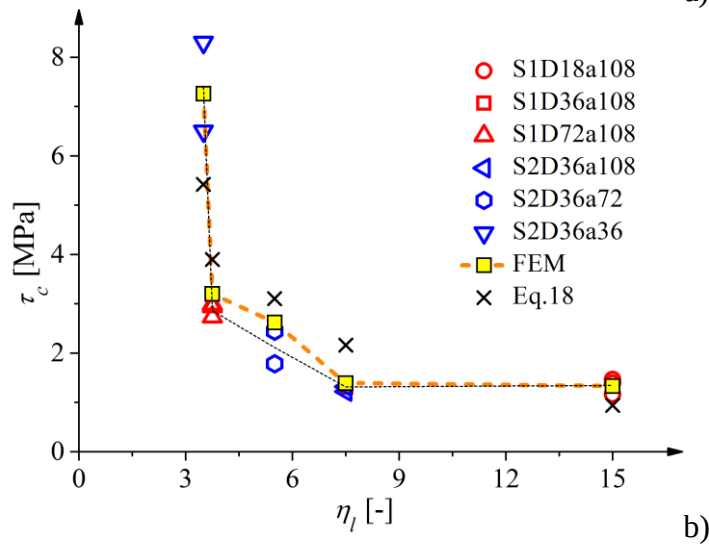
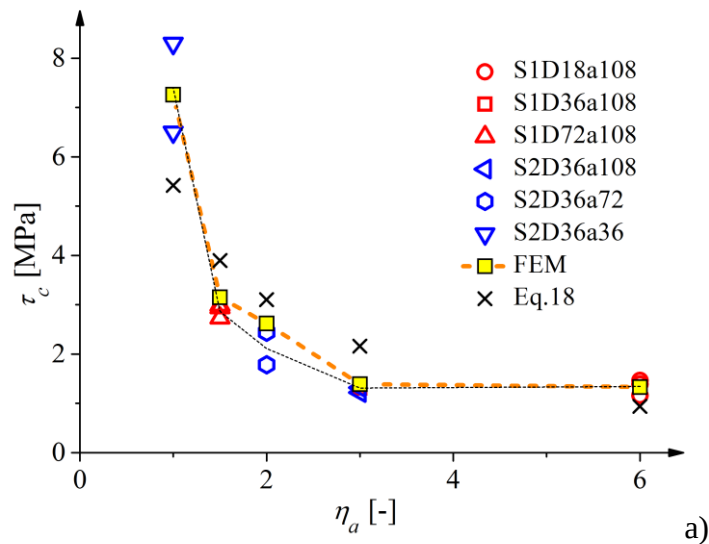


Fig.11: Shear strength τ_c from experiments, calculations and Eq.18: a) for varying shear span parameter $\eta_a=a/D$ and b) for varying length parameter $\eta_l=l_{eff}/D$ (note that beams S1D18a108 for $\eta_a=6$ failed in flexural mechanism)

FIGURE 11

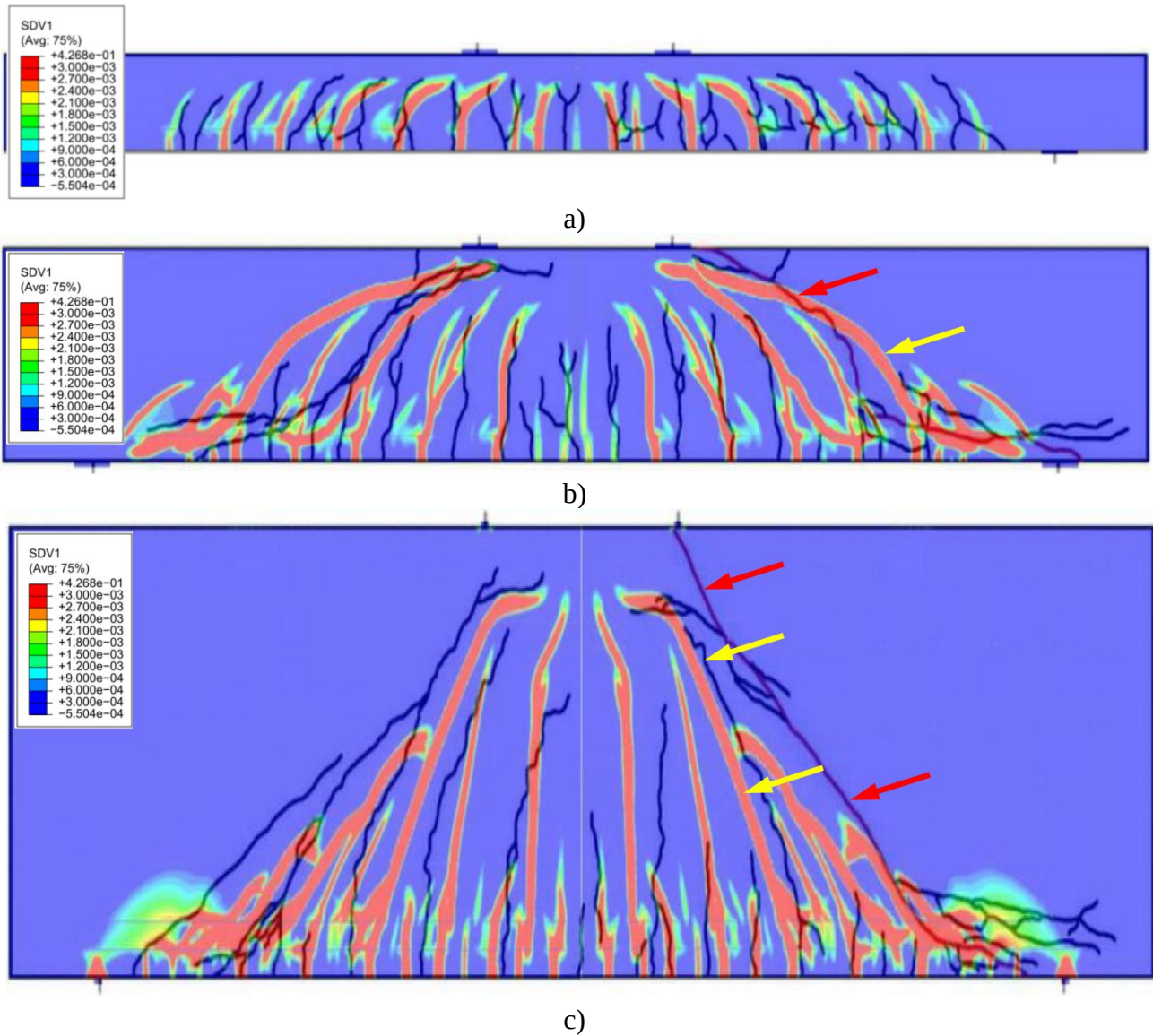
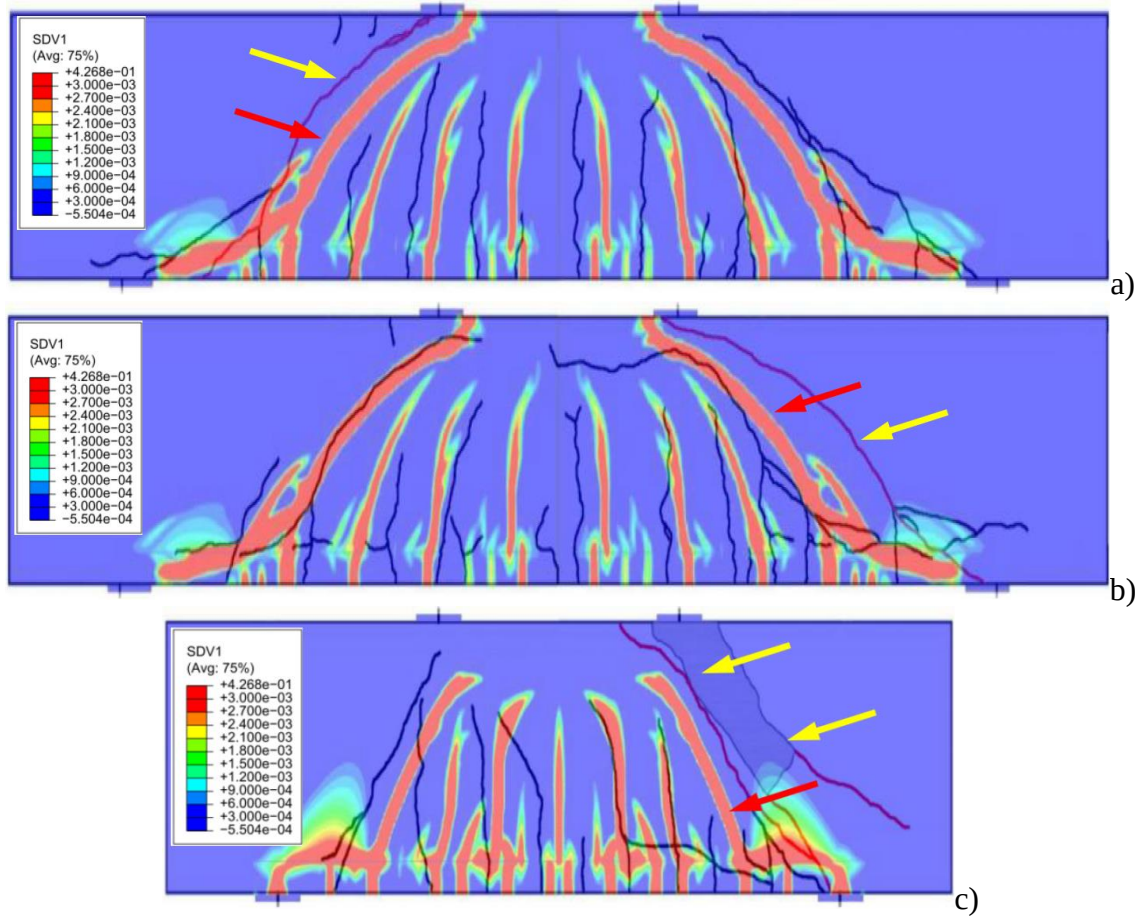


Fig.12: Contours of non-local equivalent strain measure $\bar{\epsilon}$ with attached scale as compared with experimental cracks pattern for beams of series I ($L_{eff}=2700$ mm): a) S1D18a108 ($D=180$ mm, $a=1080$ mm, $\eta_l=15$, $\eta_a=6$), b) S1D36a108 ($D=360$ mm, $a=1080$ mm, $\eta_l=7.5$, $\eta_a=3$) and c) S1D72a108 ($D=720$ mm, $a=1080$ mm, $\eta_l=3.75$, $\eta_a=1.5$) (experimental critical diagonal crack is marked by red arrow, numerical critical localization zone is marked by yellow arrow, note that beams are not proportionally scaled and steel bars are not shown)

FIGURE 12

1078
1079
1080



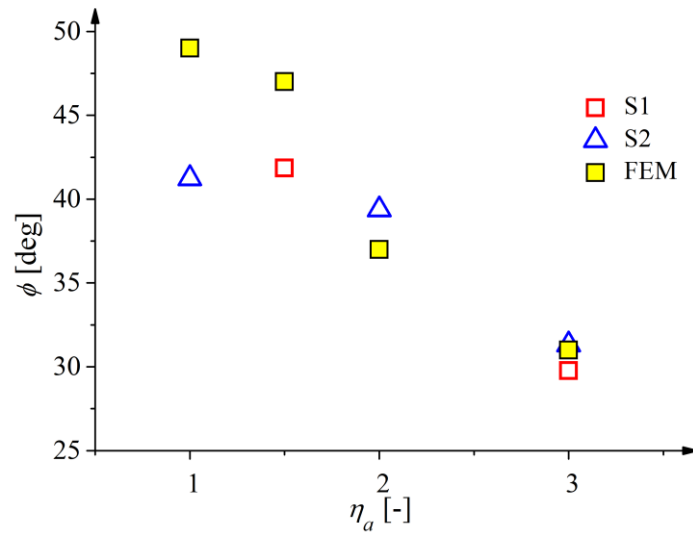
1081
1082
1083
1084
1085
1086
1087

Fig.13: Contours of non-local equivalent strain measure $\bar{\epsilon}$ with attached scale as compared with experimental cracks pattern for beams ($D=360$ mm): a) S2D36a72_1 and b) S2D36a72_2 ($L_{eff}=1980$ mm, $a=720$ mm, $\eta_l=5.5$, $\eta_a=2$) and c) S2D36a36 ($L_{eff}=1260$ mm, $a=360$ mm, $\eta_l=3.75$, $\eta_a=1$) (experimental critical diagonal crack is marked by red arrow, numerical critical diagonal localization zone is marked by yellow arrow, note that beams are not proportionally scaled and steel bars are not shown)

FIGURE 13

1088
1089

1090
1091
1092
1093
1094



1095
1096
1097
1098
1099
1100
1101
1102
1103
1104
1105

Fig.14: Diagonal failure crack/localized zone inclination ϕ to horizontal in RC beams for experimental series '1' (S1, square markers) and '2' (S2, triangle markers) versus ratio η_a as compared with FEM

FIGURE 14

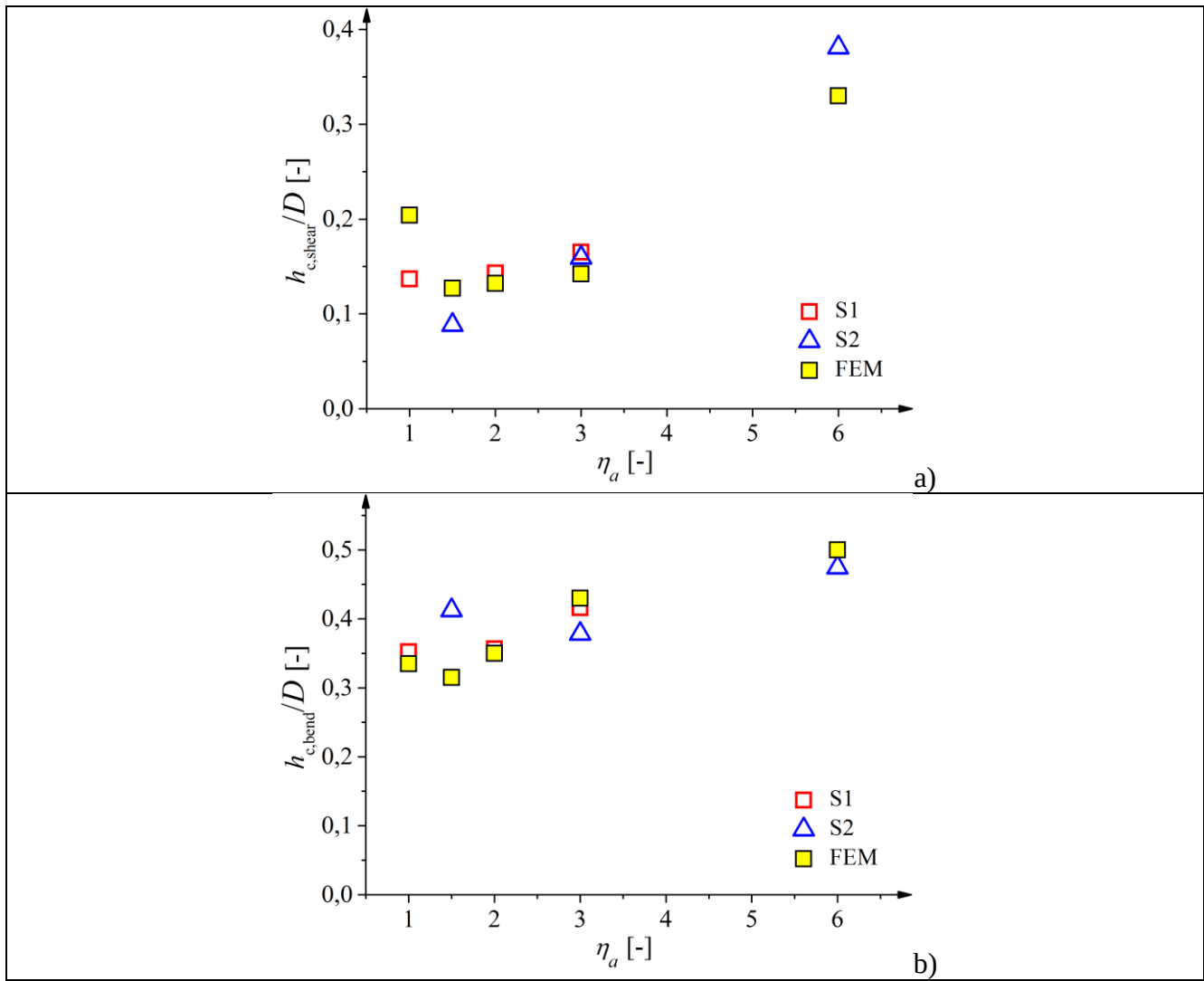


Fig.15: Experimental and calculated normalized height of compressive zone above shear and bending crack/localized zone for varying shear span parameter $\eta_a = a/D$ (S1 - experimental series '1', S2 - experimental series '2', note that beams for $\eta_a = 6$ failed in flexural mechanism)

FIGURE 15

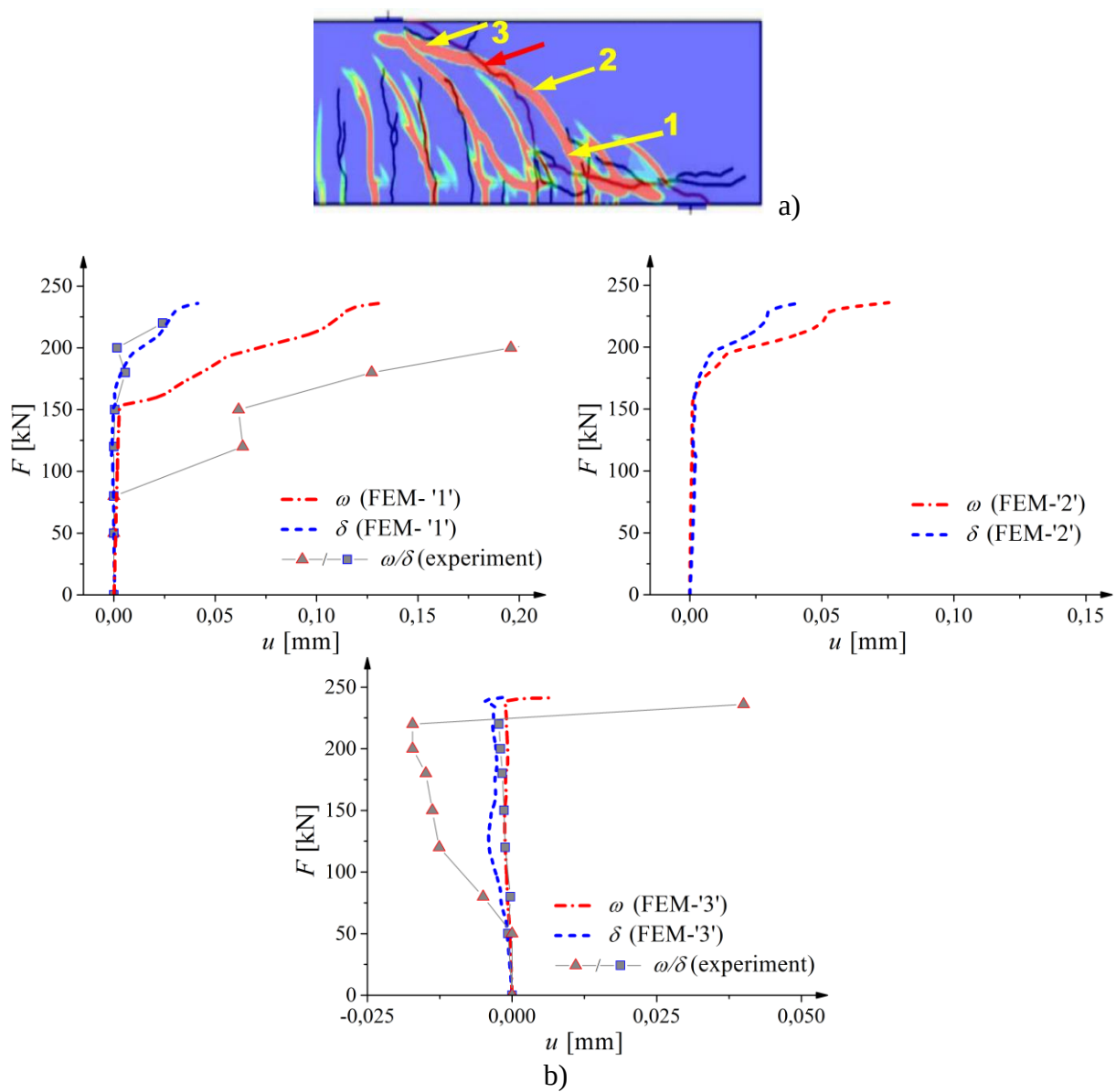
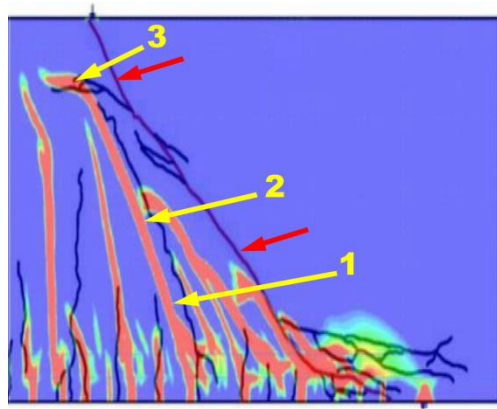
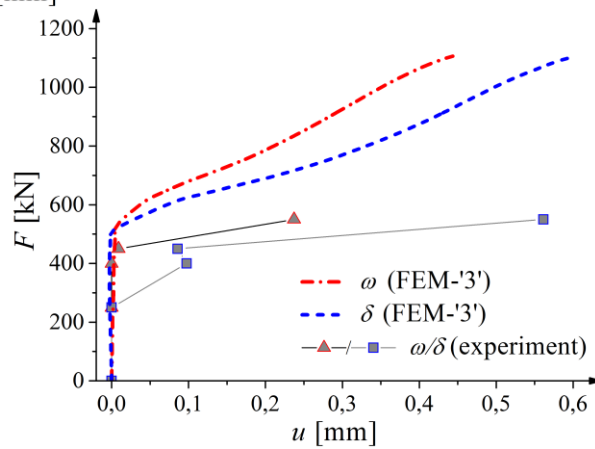
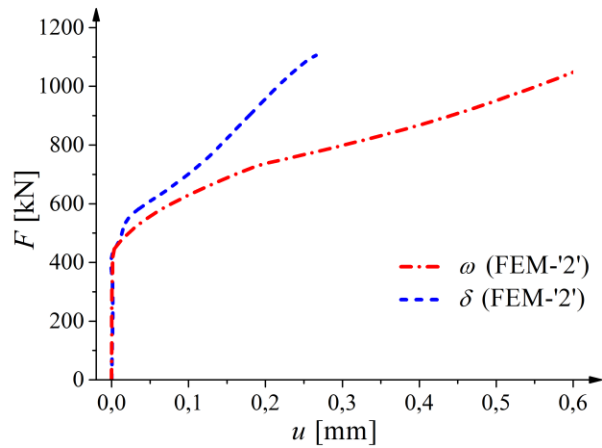
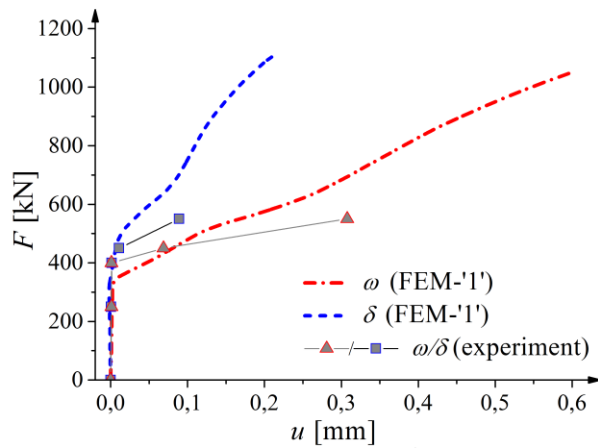


Fig.16: Calculated evolution of normal and tangential displacements at critical diagonal localization zone from FEM for beam S1D36a108 ($\eta_a=3$) as compared to experiments: a) locations (marked by yellow arrows) and b) vertical force versus displacements: ω - normal displacement, δ - tangential displacement (experimental critical diagonal crack is marked by red arrow)

FIGURE 16



a)



b)

Fig.17: Calculated evolution of normal and tangential displacements at critical diagonal localization zone from FEM for beam S1D72a108 ($\eta_a=1.5$) as compared to experiments: a) locations (marked by yellow arrows) and b) vertical force versus displacements: ω - normal displacement, δ - tangential displacement (experimental critical diagonal crack is marked by red arrow)

FIGURE 17

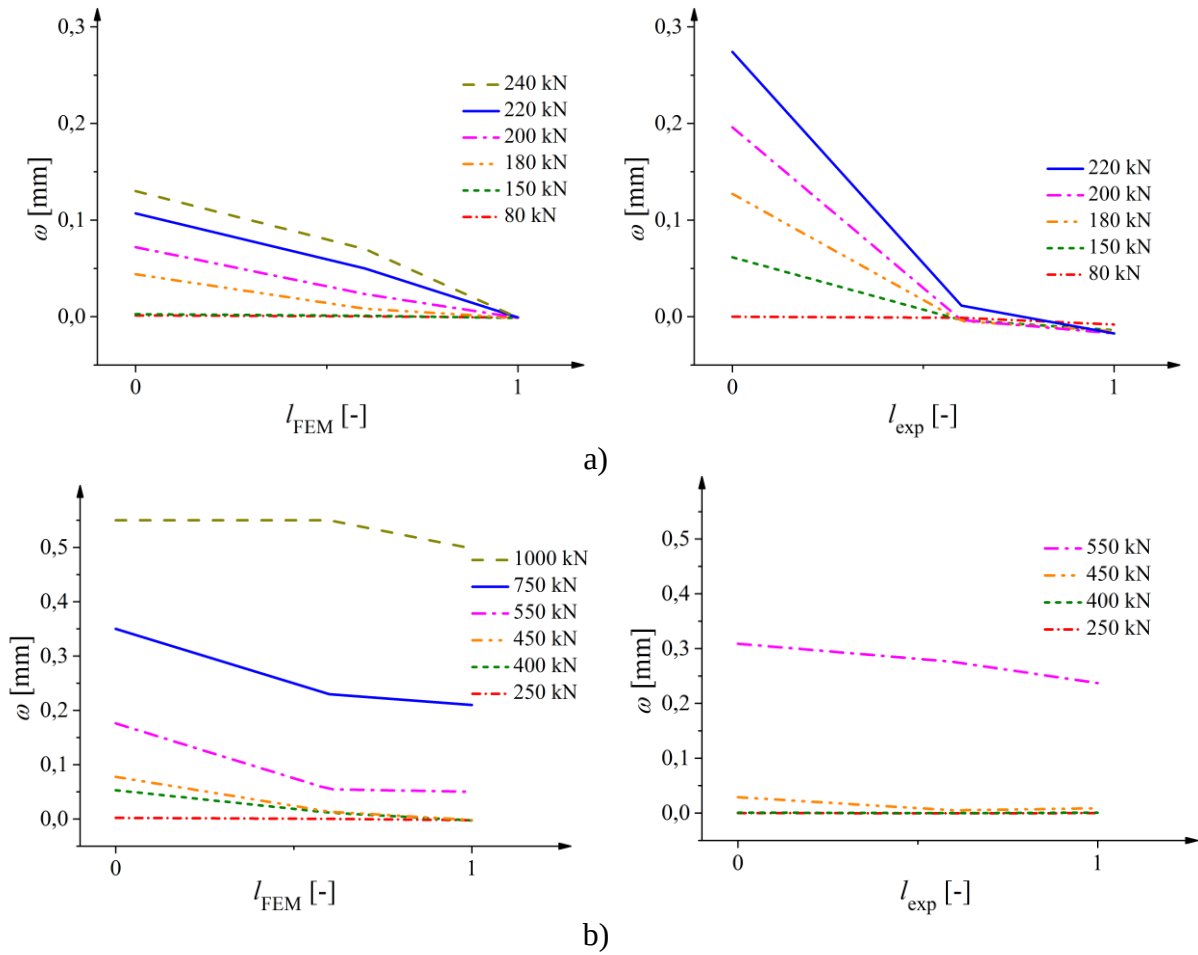
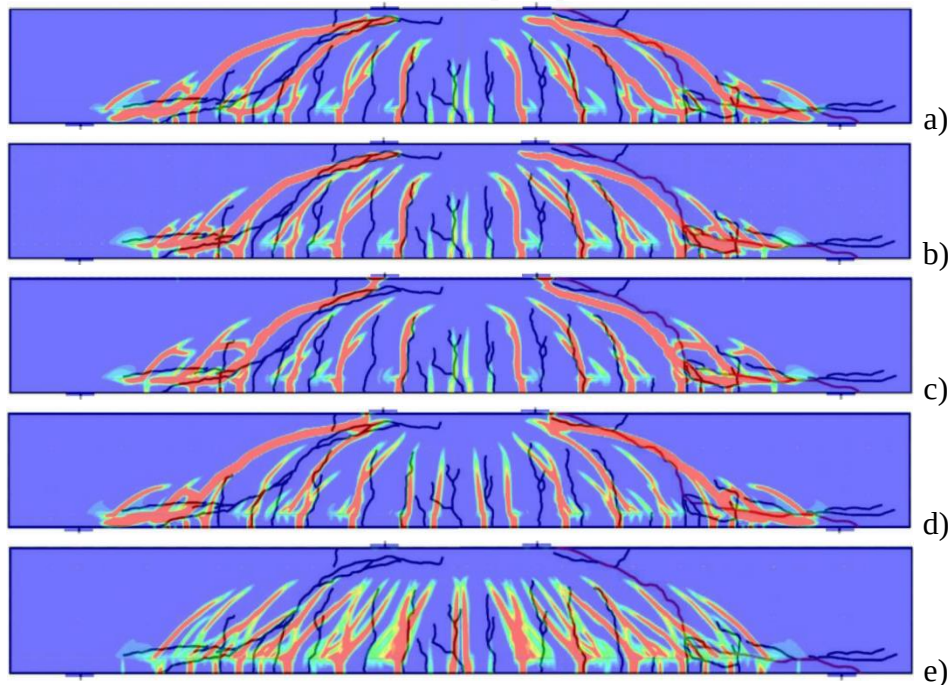
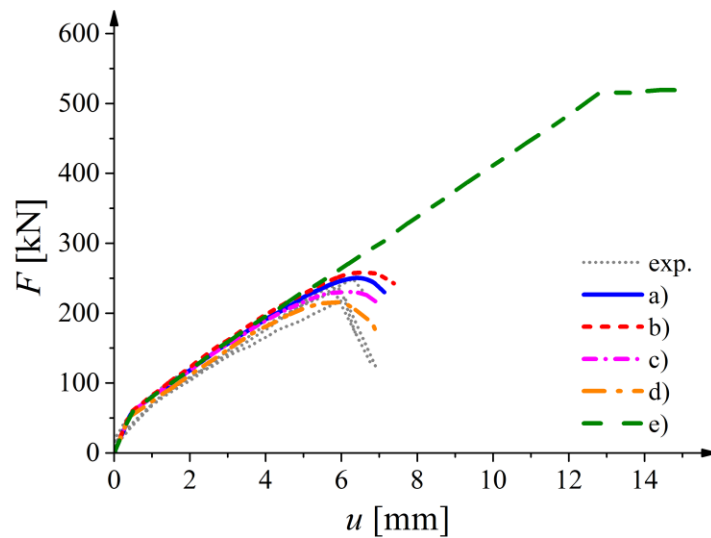


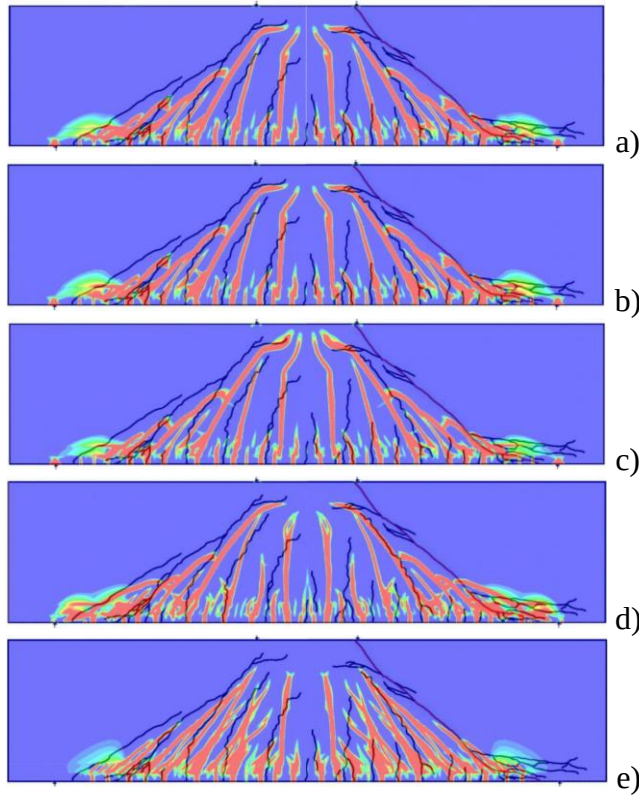
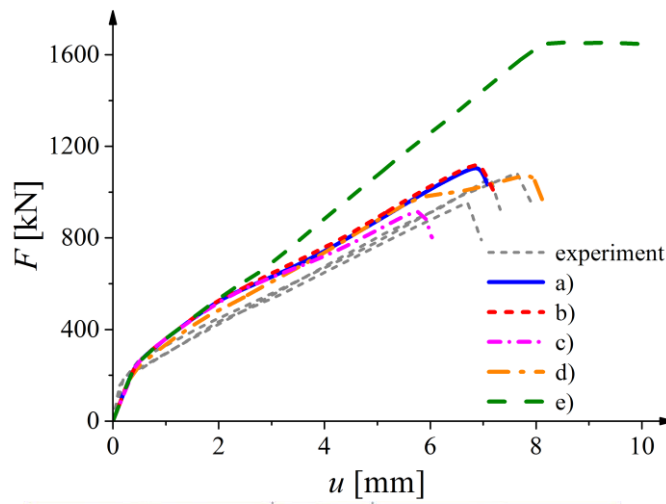
Fig.18: Comparison between calculated (left side) and experimental (right side) normal displacements w along normalized critical diagonal crack/localization zone length l_{exp}/l_{FEM} for: a) beam S1D36a108 and b) beam S1D72a108 (horizontal coordinate 0 - point above reinforcement (point '1' in Figs.16 and 17) and horizontal coordinate 1 - point in upper beam region (point '3' in Figs.16 and 17)).

FIGURE 18



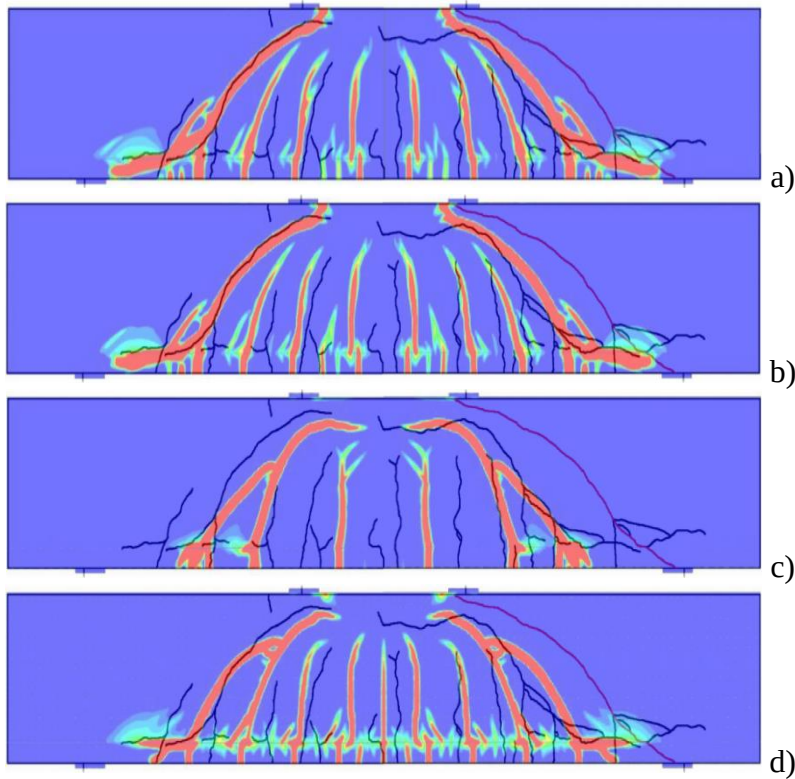
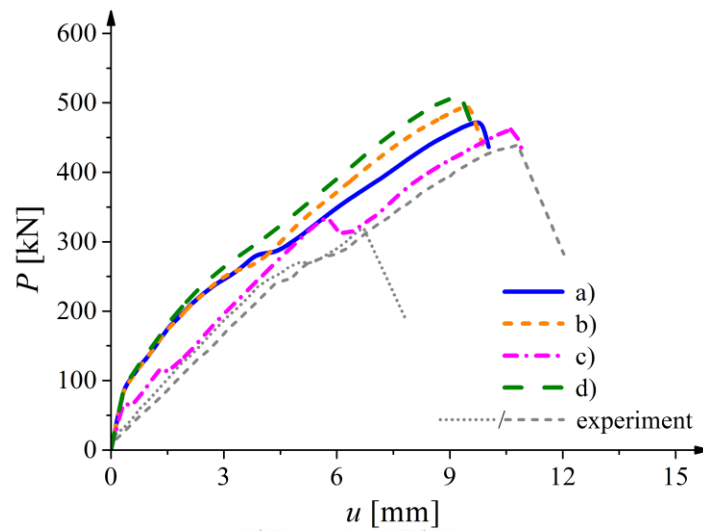
141 **Fig.19:** Calculated force-deflection curves and distributions of non-local equivalent strain measure from
 142 FE analyses using coupled elasto-plastic-damage with non-local softening as compared to experiments
 143 (beam S1D36a108, $\eta_a=3$): a) with basis set of material constants in Section 4, b) with softening constant
 144 $\beta=60$ (instead of $\beta=85$), c) with softening constants $\eta_2=0.20$ and $\delta_c=250$ (instead of $\eta_2=0.15$ and $\delta_c=150$)
 145 d) with $\kappa_0=7 \times 10^{-5}$ (instead of $\kappa_0=9 \times 10^{-5}$) and e) without plasticity and damage under compression
 146

FIGURE 19



148 **Fig.20:** Calculated force-deflection curves and distributions of non-local equivalent strain measure from
 149 FE analyses using coupled elasto-plastic-damage with non-local softening as compared to experiments
 150 (beam S1D72a108, $\eta_a=1.5$): a) with basis set of material constants in Section 4, b) with softening constant
 151 $\beta=60$ (instead of $\beta=85$), c) with softening constants $\eta_2=0.20$ and $\delta_c=250$ (instead of $\eta_2=0.15$ and $\delta_c=150$),
 152 d) with $\kappa_0=7 \times 10^{-5}$ (instead of $\kappa_0=9 \times 10^{-5}$) and e) without plasticity and damage under compression

FIGURE 20



157 **Fig.21:** Calculated force-deflection curves (dotted line – experiments) and distributions of non-local
 158 equivalent strain measure from FE analyses using coupled elasto-plastic-damage with non-local
 159 softening as compared to experiments (beam S2D36a72, $\eta_a=2$) for bond-slip model of Fig.8: a) Eq.17
 160 with $\delta_1=1$ mm, $\delta_2=2$ mm, and $\delta_3=5$ mm (basic data), b) Eq.17 with $\delta_1=0.5$ mm, $\delta_2=1.5$ mm and
 161 $\delta_3=4.5$ mm, c) Eq.17 with $\delta_1=100$ mm, $\delta_2=200$ mm and $\delta_3=500$ mm and d) perfect bond model

2
 3 **FIGURE 21**

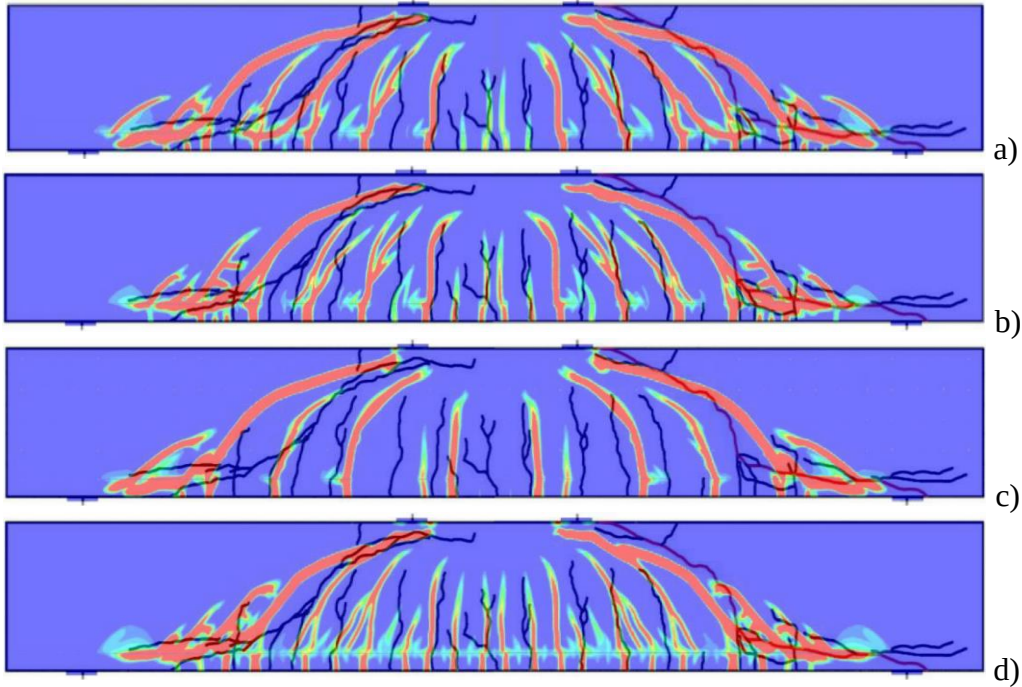
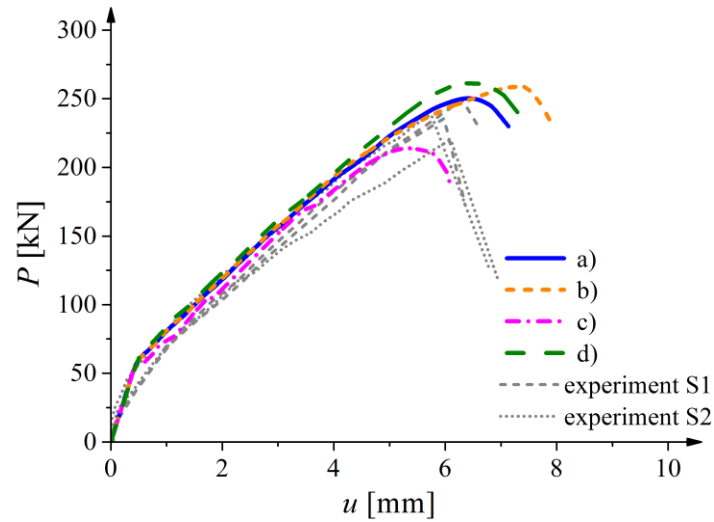


Fig.22: Calculated force-deflection curves (dotted line – experiments) and distributions of non-local equivalent strain measure from FE analyses using coupled elasto-plastic-damage with non-local softening as compared to experiments (beam S1D36a108, $\eta_a=3$) for bond-slip model of Fig.8: a) Eq.17 with $\delta_1=1$ mm, $\delta_2=2$ mm, and $\delta_3=5$ mm (basic data), b) Eq.17 with $\delta_1=0.5$ mm, $\delta_2=1.5$ mm and $\delta_3=4.5$ mm, c) Eq.17 with $\delta_1=100$ mm, $\delta_2=200$ mm and $\delta_3=500$ mm and d) perfect bond model

FIGURE 22